Thermodynamic modelling of liquids: CALPHAD approaches and contributions from statistical physics

Thermodynamic modelling of liquids: CALPHAD approaches and contributions from statistical physics

Chandler A. Becker[*,1] , John Agren[◦2] , Marcello Baricco[3], Qing Chen[4] , Sergei A. Decterov[5] , Ursula R. Kattner[1], John H. Perepezko[6] , Gernot R. Pottlacher[7] , and Malin Selleby[2]

[1] Materials Science and Engineering Division, National Institute of Standards and Technology, Gaithersburg, MD 20899, USA

[2] KTH Royal Institute of Technology, Department of Materials Science and Engineering, 10044 Stockholm, Sweden

[3] Department of Chemistry and NIS, University of Turin, 10125 Torino, Italy

[4] Thermo-Calc Software AB, 11364 Stockholm, Sweden

[5] Department de Genie Chimique, Ecole Polytechnique, CRCT, Montreal,` PQ H3C 3A7, Canada

[6] Department of Materials Science and Engineering, University of Wisconsin-Madison, Madison, WI 53706, USA

[7] Graz University of Technology, Institute of Experimental Physics, 8010 Graz, Austria

Keywords CALPHAD, first-principles, glass transition, liquids, molecular dynamics, thermodynamic modelling

Abstract

We describe current approaches to thermodynamic modelling of liquids for the CALPHAD method, the use of available experimental methods and results in this type of modelling, and considerations in the use of atomic-scale simulation methods to inform a CALPHAD approach. We begin with an overview of the formalism currently used in CALPHAD to describe the temperature dependence of the liquid Gibbs free energy and outline opportunities for improvement by reviewing the current physical understanding of the liquid. Brief descriptions of experimental methods for extracting high-temperature data on liquids and the preparation of undercooled liquid samples are presented.

Properties of a well-determined substance, B_2O_3, including the glass transition, are then discussed in detail to emphasize specific modelling requirements for the liquid. We then examine the two-state model proposed for CALPHAD in detail and compare results with experiment and theory, where available. We further examine the contributions of atomic-scale methods to the understanding of liquids and their potential for supplementing available data. We discuss molecular dynamics (MD) and Monte Carlo methods that employ atomic interactions from classical interatomic potentials, as well as contributions from *ab initio* MD. We conclude with a summary of our findings.

1 Introduction Although few inorganic materials are used in their liquid state, liquids play an important role in the manufacture of many materials. This can be either because they are processed from the liquid or, for fulfilling performance criteria, the formation of the liquid phase must be avoided. Additionally, there are now a number of commercially available amorphous solids, both in the form of oxides and metallic glasses, and accurate descriptions of these sys-tems are necessary over a wide range of temperatures. How-ever, liquid phases of many inorganic substances are only sta-ble at high temperatures where the experimental determination of their properties is more challenging than at lower tem-peratures. Many amorphous phases are, at best, metastable and their properties can be difficult to measure. In addition, the data from glassy phases cannot be directly applied to modelling liquids because they have gone through the glass transition, with the attendant sharp drop in heat capacity. As a result, the experimental data for generating and evaluating models of liquids and glasses are fairly sparse. This has a significant impact on the development and refinement of models that strongly depend on the availability of thermodynamic data, such as those needed in CALPHAD modelling.

CALPHAD is one of the major ways to model the thermodynamics of liquids. However, for many systems, especially the unaries (elements and sometimes compounds), the data necessary to develop, parameterize and validate models are limited. Theoretical approaches, e.g. first-principles or classical atomistic simulation, can help provide data

and mechanistic understanding, but these methods are not commonly applied to CALPHAD modelling of liq-uids. Additionally, there are known problems with existing descriptions used in CALPHAD for undercooled liquids and amorphous solid phases. Addressing these issues was the charge given to the 'Liquids' group at the 2013 Ring-berg Unary Workshop with the ultimate goal of assessing and developing better models of liquids in CALPHAD. Specifically this group was charged with determining how modelling of liquids might be improved, how limitations of the current CALPHAD models might be overcome, and with examining whether and how atomic-scale methods (such as first-principles calculations or atomistic simulation) might be used to inform or provide data on liquids for use in CAL-PHAD assessments.

We will begin by reviewing the current understanding of liquids and discussing some of the limitations of the current CALPHAD approach to provide context for the remaining sections. The SGTE database [1] is the main source of elemental thermodynamic descriptions currently used in CALPHAD. This set of descriptions has two major shortcomings. One is that the extrapolation of the thermodynamic functions to temperatures below the melting point does not give meaningful values for entropy and heat capacity, and, therefore, these functions are not a good basis for the description of glassy or amorphous alloys. The other shortcoming is that these functions have artificial break points (kinks) in entropy and heat capacity functions at the melting point of the pure elements, and these break points remain as artefacts in the description of multi-component alloy liquids. When the formalism of SGTE was first presented as an 'interim' solution more than two decades ago, these shortcomings were accepted to avoid more pronounced problems during the extrapolation to metastable temperature regimes. In 1995, a workshop was organized at Ringberg to develop models for the description of the unary data that would overcome these shortcomings. One of the groups at this workshop focussed on the extrapolation of the heat capacity in liquid and amorphous phases [2]. However, only a few descriptions of the elements were developed using the recommendations from this workshop.

Given that the description of undercooled liquids for unaries suggested by the SGTE database [1] is still unsatis-factory to describe the thermodynamics of liquid/amorphous phases, our goal was to treat the heat capacity, $\boldsymbol{C}_{\mathrm{P}}$, for liquid and solid amorphous phases from high temperatures (defined as 2000 K at the workshop) to low temperatures, ideally 0 K. Formalisms should accommodate the thermodynamics associated with any liquid–glass transitions and be able to handle effects of high pressure. Ideally temperatures should extend up to the melting temperature of tungsten.
Additionally, any CALPHAD liquid formalisms should be as physically grounded as possible.

We note here that a strict definition of a unary is that it is a system consisting of one element. However, a unary is also frequently defined as a system consisting of a com-pound with fixed composition under conditions for which it does not decompose into other components [3]. Because of the relatively limited availability of experimental data for liquid pure elements, especially in the undercooled state, we expanded the scope to also include compound unaries in the discussions. In addition, including these compound unaries also allowed the discussion of the glass transition that is more commonly observed in these systems.

First, we will discuss the current understanding of the liquid and give a detailed discussion of the issues by focussing on the case of B_2O_3. We will then focus on the two-state model proposed in 1988 by Agren [4] for undercooled liquids and applied in 1995 by Agren et al. [2] to the description of the liquid at temperatures up to 5000 K and multi-component systems. We will then finish with some considerations in the use of theoretical data (particularly classical atomistic simulation) as part of a CALPHAD framework, followed by a summary of the paper.

2 Current understanding of liquids The behaviour of liquids needs to be captured from well above the melting temperatures to significantly below. Here we will describe aspects of the current understanding of both liquids and glasses that are particularly relevant for CALPHAD modelling. Of particular note is the following: one of the challenges in modelling the liquid/amorphous phase is that data suggest that, for many unaries, the heat capacity is constant above the melting point. However, extrapolation of this constant behaviour to temperatures far below the melting point may result in values for the entropy that are physically unrealistic.

2.1 Liquids above and below $T_{\mathbf{M}}$ Experimental and theoretical studies of liquids suggest that the heat capacity, $\boldsymbol{C}_{\mathrm{P}}$, is constant above the melting point. Grimvall [5] analyzed the temperature dependence of the heat capacity of several low-melting metals and concluded that there is a gradual transition in $\boldsymbol{C}_{\mathrm{V}}$ from the Dulong–Petit value of $3\boldsymbol{R}$ towards $2\boldsymbol{R}$ as the temperature increases above the equilibrium melting point.

Molecular dynamics (MD) simulations, whether based on classical interatomic potential models, or on density-functional-theory (DFT) energies and forces (so-called *ab initio* MD, or AIMD) have been extensively used to study the properties of the liquid. Previous MD studies have found the enthalpy of liquids to be roughly linear above the melting temperature. This leads to a small, if any, temperature dependence for the constant-pressure heat

capacity (C_P) of liquids well above the melting temperature for $P \approx 0$. Sadigh and Grimvall [6] and Forsblom and Grimvall [7] gave detailed treatments of the relationships between C_P , C_V, and compressibility and thermal expansion, and then applied them to Cu and Al melts, respectively. Brown and Adams [8] also found a linear relationship between enthalpy and temperature for the Cu melt. For Al, the enthalpy was generally found to be linear in the liquid, but this was not true for all interatomic potentials describing Al [9]. The relatively constant values of C_P for the liquid have been explained as a consequence of the competition between thermal expansion and a gradual loss of shear resistance with increasing temperature [7].

However, a scarcity of data (experimental and theoretical) makes it difficult to generally understand the heat capacity in undercooled liquids or how to address the transition from undercooled liquids to glasses, where appropriate. Heat capacity data for undercooled liquids have been published for low-melting elements (Ga [10, 11], In, Bi, Sn [12] and Se [13, 14]) and several high-melting metals (Au, Cu, Ag [15]). Experimental determination of C_P is usually performed by calorimetry [16]. However, conventional methods are usually limited to temperatures below 1000 $^\circ$ C. Detailed descriptions of the experimental methods that can be used to extract high-temperature data on liquids are given in Appendix A. Measurements of undercooled liquids pose special challenges. For example Perepezko and Paik [12] used specially prepared droplets for the measurement of undercooled In, Bi and Sn liquids. A brief synopsis of undercooled liquid sample preparation is also given in Appendix A. Limited MD results for the heat capacity of Ni [17] and Au (in Au–Cu) [18] liquids are available for temperatures above and below T_M. A review of atomistic simulations of undercooled liquid alloys is in Ref. [19].

Besides examining thermodynamic quantities, such as the heat capacity, atomic-scale simulation can also be used to understand structure at the nanoscale to help interpret thermodynamic and kinetic modelling. In particular, short range order (SRO) in liquids has been studied extensively for both elements and alloys. As an example, Jakse and Pas-turel [20, 21], found ordering in liquid Ni using both *ab initio* molecular dynamics (AIMD) and classical MD with more complex ordering appearing with lower temperatures in the undercooled liquid. These methods will be discussed, along with an example for Au and Ni liquids, in Section 6.

2.2 Glasses and the glass transition More than half a century ago Kauzmann [22] discussed the behaviour of several rather different liquids that were undercooled below their equilibrium crystallization temperature. The liquids spanned from oxides like B_2O_3 (discussed in detail in the next section) to organics like glycerol and had in common that it was reasonably easy to obtain rather large undercooling, i.e. 30–40% below the melting temperature, without crystallization. Kauzmann found that all liquids have a similar behaviour; upon cooling they lower their entropy more than the crystalline phase, i.e. their heat capacity is higher than that of the crystal. Kauzmann pointed out that if crystallization could be bypassed there would be a temperature below which the liquid would have much lower entropy than the crystalline phase, which he regarded as a paradox. Moreover, he concluded that in reality this would not happen because there is a glass transition below which the liquid structure is 'frozen-in' at a higher entropy. Although he quite clearly stated that the glass transition is a relaxation phenomenon he speculated that there could be some under-lying thermodynamic transition. Much later when metallic glasses were discovered the behaviour of undercooled metallic liquids became experimentally accessible. Chen and Turnbull [23] reported heat capacity measurements of a glass-forming Au–Ge–Si alloy in the undercooled as well as in the glassy state. The behaviour they observed was remarkably similar to that reported by Kauzmann.

We can summarize the generic behaviour as follows. As a liquid is cooled from high temperature there is a gradual change to a more solid-like behaviour. This change is revealed in the variation of thermodynamic properties, e.g. a loss of entropy and an increase in heat capacity. It has been found that C_P between the undercooled liquid and the glass for many metallic systems is, on average, approximately 13.69 ± 2.05 J mol^{-1} K^{-1} at the glass transition temperature [24]. However, glass formation is basically a kinetic phenomenon. Several approaches have been suggested to connect thermodynamic and kinetic parameters of glasses, e.g. fragility and entropy [25]. The glass transition temperature is strongly influenced by the quenching rate used to prepare the glass and by the heating rate used to obtain it. Therefore, the glass transition temperature cannot be directly determined by thermodynamic calculations.

The physics of glassy states is still under discussion. A 'potential energy landscape' (PEL) has been suggested for the glassy state [26–29]. Theories suggest the occurrence of a multi-stage state for atoms/molecules in a glass. In the past, simpler models based on free volume theory of liquids have been suggested (for a review see [30]). In particular, a continuous transformation from 'liquid-like' to a 'solid-like' behaviour of undercooled liquids has been suggested during glass formation [31]. These phenomena have been discussed more recently by Angell and Moynihan [32]. This model (two-state) has been applied to the calculation of thermodynamic properties by Agren [4]. Later it was suggested by the Ringberg group in 1995 for the description of undercooled liquids in unaries [2]. This approach will be discussed in more detail later in the paper.

Two-state models are also found in MD simulations of liquids and amorphous phases. Hao et al. [33] developed a model of metallic glass transitions using a two-state approach where the fractions of atoms in ordered (icosahedral) and

disordered (non-icosahedral, liquid-like) structures depend on the free energy differences between the ordered and disordered states. There is also a 'frustration' parameter in the model that reflects the constraint that, due to local environmental constraints, not all atoms can transition from one state to the other. This model exhibits different fractions of ordered and disordered clusters as a function of cooling rate, as observed in other MD simulations, and it addresses one challenge associated with comparing MD simulation results with experiment, namely the dramatic differences in cooling rates achievable in MD and in experiment.

Another two-phase approach was developed in the two-phase thermodynamic (2PT) model described in Ref. [34]. In that model, the vibrational density of states (DoS) for a liquid is broken into gas- and solid-like contributions, which is conceptually similar to the two-state approach for CAL-PHAD modelling. From the Fourier transform of the velocity autocorrelation function, quantities such as the free energy and entropy can then be calculated. This approach has been applied to glass formation in Al–Ni [35], and Cu–Zr–Al alloys [36].

Glasses and glass transitions have been studied extensively with MD. While a comprehensive review is outside the scope of this paper, Cheng and Ma [37] published a thorough review of metallic glass research in 2011.

Amorphous phases have already been described in the framework of a CALPHAD approach. The first description was suggested by Bormann [38, 39]. It was based on the Kauzmann paradox [22], (i.e. vanishing $\boldsymbol{S}^{l-s}$ at $\boldsymbol{T}_K$). On the basis of the hole theory of liquids, the $\boldsymbol{C}_P$ of undercooled liquid was considered proportional to $\boldsymbol{T}^{-2}$. Later, a second order transformation was considered for the glass transition. The equation for ferromagnetic transformations (IHJ model) was borrowed to describe glass transitions [40]. This model has been applied to several binary systems. For a review of CALPHAD descriptions for glass forming systems, see Refs. [41, 42].

3 Detailed discussion of B_2O_3 Extrapolation of the heat capacity of a stoichiometric liquid compound below its melting temperature is important for two reasons. On the one hand, liquid solutions are often stable below the melting points of pure components, so $\boldsymbol{C}_P$ of a solution is normally evaluated from the extrapolated $\boldsymbol{C}_P$ values, using the Neumann–Kopp rule (Eq. (1), below) as a first approximation. On the other hand, there is a need to describe thermodynamic properties of glasses and amorphous materials, and it is often assumed that these properties can be obtained by extrapolation of the properties of the liquid phase to lower temperatures.

The behaviour of $\boldsymbol{C}_P$ below the melting temperature can be best illustrated by using a well-known glass-forming oxide, B_2O_3, as an example. The heat capacity of this oxide was studied experimentally over the whole temperature range from above the melting point to room temperature [43–45]. The experimental data are shown in Fig. 1. The calculated line was obtained in the assessment of Decterov et al. [46] and is based not only on heat capacity measurements, but also on heat content data. As can be seen from Fig. 1, the heat capacity of liquid B_2O_3 is constant from 550 to 900 K within the experimental scatter. At lower temperatures it rapidly drops and becomes equal to $\boldsymbol{C}_P$ of crystalline B_2O_3. The drop occurs over a relatively narrow temperature range, which is normally referred to as the glass transition temperature, $\boldsymbol{T}_g$. The measured values are somewhat different for the cool-ing and heating experiments and depend on the cooling and heating rate, so that $\boldsymbol{T}_g$ is an important material characteristic governed not only by thermodynamics but also kinetics. It

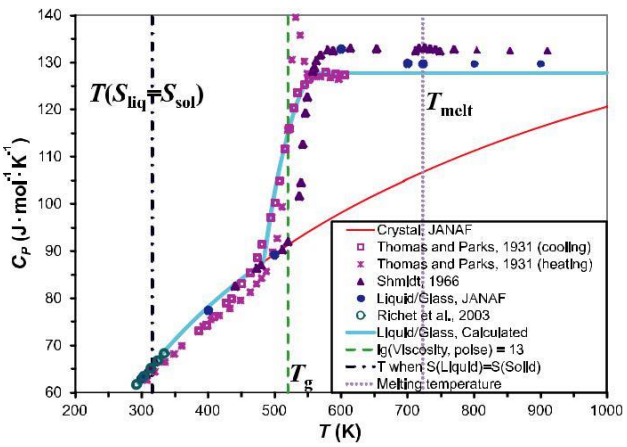

Figure 1 Heat capacity of solid, liquid and glass B_2O_3. $\boldsymbol{T}_{melt}$ is the melting temperature, $\boldsymbol{T}_g$ is the temperature corresponding to the viscosity of B_2O_3 equal to 10^{12} Pa s and $\boldsymbol{T}$ ($\boldsymbol{S}^{liq} = \boldsymbol{S}^{sol}$) is the Kauzmann temperature.

is commonly inferred that upon cooling below the freezing point, molecular motion slows down and around the glass transition temperature liquid loses translational degrees of freedom. The liquid structure therefore appears 'frozen' on the laboratory timescale and the heat capacity originating from the vibrational degrees of freedom is similar to that of the solid phase.

The origin of the maximum that is normally observed on a heating curve at the glass transition region can be easily understood from the enthalpy curves shown in Fig. 2. When glass is heated, the enthalpy increases, staying parallel to the enthalpy of the corresponding solid phase, because the heat capacities of the solid and glass phases are essentially the same. Since the heating is not infinitely slow, the translational degrees of freedom remain 'frozen' on the laboratory timescale and the glass inevitably gets somewhat overheated

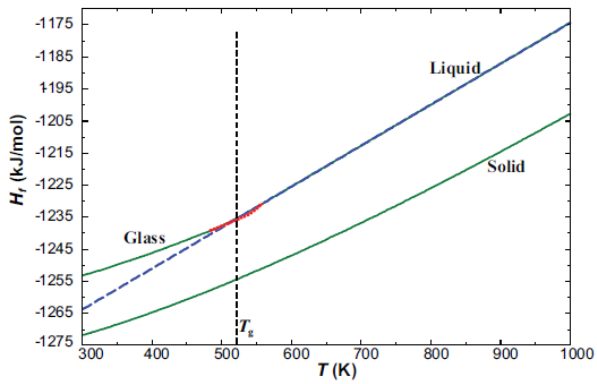

Figure 2 Enthalpy of formation of solid, liquid and glass B_2O_3. $\boldsymbol{T}_g$ is the temperature corresponding to the viscosity of B_2O_3 equal to 10^{12} Pa s. The dashed line is calculated assuming that $\boldsymbol{C}_P$ of liquid remains constant at all temperatures. The dotted line illustrates the enthalpy change for a heating curve.

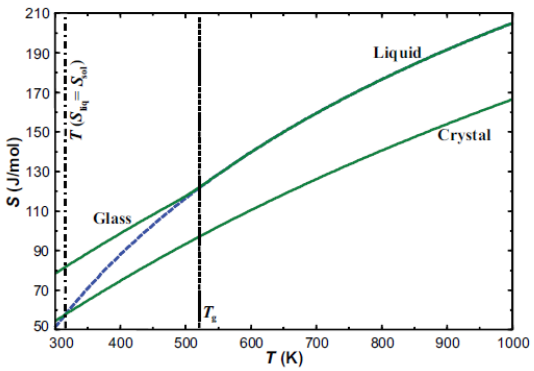

Figure 3 Entropy of solid, liquid and glass B_2O_3. $\boldsymbol{T}_g$ is the tem-perature corresponding to the viscosity of B_2O_3 equal to 10^{12} Pa s and $\boldsymbol{T}$ (S^{liq} =S^{sol}) is the Kauzmann temperature. The dashed line is calculated assuming that $\boldsymbol{C}_P$ of liquid remains constant at all temperatures.

when going through the glass transition region. This means that the enthalpy continues to move parallel to that of the solid phase (see the dotted lines in Fig. 2). However, even-tually the heating curve should join with the enthalpy curve for the liquid, and this is only possible if the apparent heat capacity, or the slope of the heating curve, becomes higher than $\boldsymbol{C}_P$ of the liquid phase and goes through the maximum.

If $\boldsymbol{C}_P$ of the liquid phase did not drop at $\boldsymbol{T}_g$ but rather continued to remain constant below this temperature, the corresponding entropy of the liquid shown by the dashed line in Fig. 3 would eventually become smaller than the entropy of the solid. In reality, this does not happen since $\boldsymbol{C}_P$ does drop at the glass transition temperature and the

entropy of the undercooled liquid remains substantially higher than the entropy of the solid phase as can be seen from Fig. 3. The Kauzmann temperature, i.e. the point at which the extrapolated S (liquid) is equal to S (solid), is about 200 K lower than the glass transition temperature defined by the temperature range where C_P of the liquid rapidly drops. It was proposed earlier and at a previous Ringberg meeting [47, 48] to take the Kauzmann temperature as an approximation for the glass transition temperature. Clearly, this is not a good assumption for B_2O_3.

In the glass industry, the glass transition temperature is normally defined as the temperature corresponding to the viscosity equal to 10^{12} Pa s (or 10^{13} poise). As can be seen from Fig. 1, the temperature obtained by this definition is in surprisingly good agreement with the temperature range where C_P of undercooled liquid drops (the viscosity was calculated using the model for oxide liquids [49], which fits the numerous experimental data on the viscosity of liquid and glass B_2O_3). The same viscosity model [49–53] was also used to estimate the glass transition temperatures for liquids with diopside ($CaMgSi_2O_6$), anorthite ($CaAl_2Si_2O_8$) and albite ($NaAlSi_3O_8$) compositions. The calculated glass transition temperatures corresponding to the viscosity equal to 10^{12} Pa s were within 50 K of the temperature ranges where the drop of C_P was reported [54]. These estimates appeared to be more accurate than the glass transition temperatures obtained experimentally from the change of slope of the heat content curves [55]. Since experimental measurements of C_P of undercooled liquids are scarce, viscosity data and models can be used to provide reasonable estimates of the glass transition temperature, at least for oxide liquids. When viscosity data are also lacking, a fairly rough estimate of T_g can be obtained from an empirical relation $T_g / T_M = 0.68 \pm 0.08$ for oxides, where T_M is the melting temperature. In pure metals, a value of 0.25 has been suggested by Turnbull [56]. This value varies significantly for alloys.

When the glass transition temperature is known, a good estimate of the thermodynamic properties of undercooled liquid and glass can be obtained by extrapolating C_P of the liquid down to T_g and by using C_P of the corresponding solid phase below T_g. If it is desirable not to have a discontinuity in the heat capacity at the glass transition temperature, one can always use an additional C_P range from $T_g - T/2$ to $T_g + T/2$ to describe a continuous decrease of C_P over the narrow interval T rather than having a vertical drop at T_g. This would have a negligible effect on the thermodynamic properties of liquid/glass and on calculated phase equilibria at all temperatures except maybe the interval T. However, this is quite an artificial function.

4 Effect of T_g and C_P extrapolations into binary solutions We explore now the effect on a hypothetical system if the C_P change at T_g were incorporated into the heat capacity function. The glass transition temperature of a solution depends on composition, which has important implications for thermodynamic modelling of solutions. This can be best illustrated by a simple example. Consider a binary system A–B in which solid A melts at 1850 K with the enthalpy of melting H_M = 19 kJ mol^{-1} and solid B melts at 2150 K with H_M = 21 kJ mol^{-1}. Let us assume that the glass transition temperatures for pure liquid A and B are 1700 and 1900 K, respectively. Let us further assume that liquid A and B form an ideal solution and that there is no solid solubility. Finally, let us use C_P functions for A and B shown in Fig. 4. These heat capacities are similar to the real values for Zr and V. For the pure liquid components, the constant heat capacity of the liquid phase is extrapolated down to the glass transition temperature and then drops to C_P of the solid. In the absence of experimental data on C_P of the liquid solution, the Neumann–Kopp rule is normally applied to evaluate the heat capacity of the solution:

$$C_p(X) = (1 - X)C_p(\mathrm{A}) + XC_p(\mathrm{B}), \qquad (1)$$

where X is the mole fraction of component B. The phase diagram calculated for the A–B system with no interaction parameters for the liquid phase is shown by the solid line in Fig. 5.

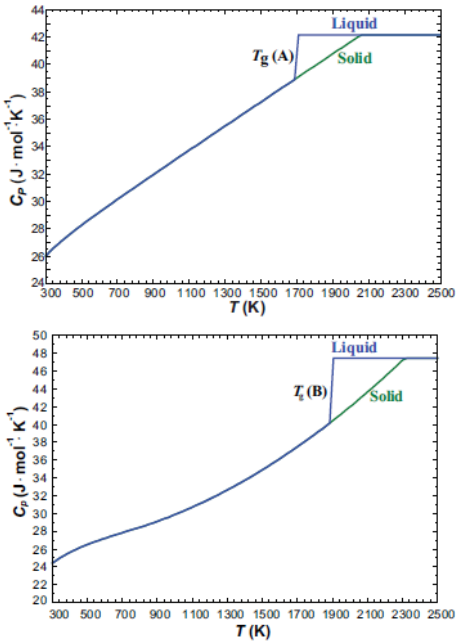

Figure 4 Heat capacities of solid and liquid pure components in the hypothetical A–B system: (a) component A, (b) component B.

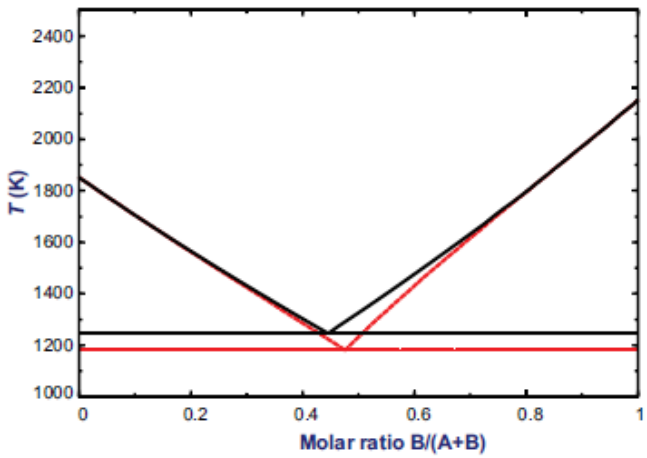

Figure 5 Phase diagram of the A–B system. $\boldsymbol{C}_P$ of the liquid phase is estimated from the pure liquid components by the Neumann– Kopp rule. The solid lines are calculated assuming that the heat capacities of the pure liquid components drop at their glass transition temperatures. The dashed lines are calculated assuming that $\boldsymbol{C}_P$ of the pure liquid components remains constant and does not drop at $\boldsymbol{T}_g$.

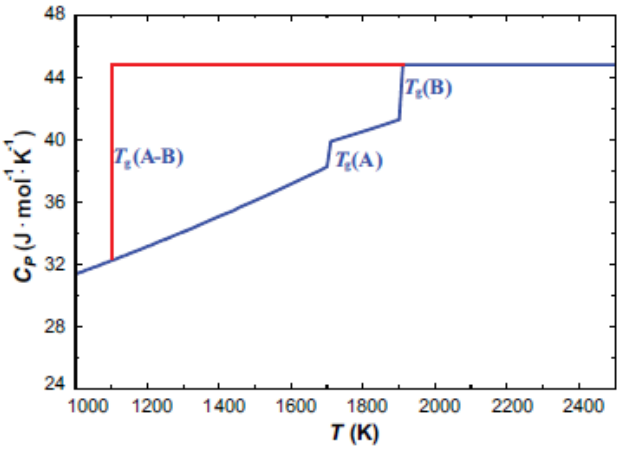

Figure 6 Heat capacity of A–B liquid at X(B) = 0.5. C_P of the liquid phase is estimated from the pure liquid components by the Neumann–Kopp rule. The solid lines are calculated assuming that the heat capacities of the pure liquid components drop at their glass transition temperatures. The dashed lines are calculated assum-ing that the heat capacities of the pure liquid components remain constant and drop only at T_g of the *solution*.

The presence of the glass transition temperatures for pure liquid components in combination with the Neumann–Kopp rule (Eq. 1) results in non-smooth C_P of the liquid solution as shown by the solid lines in Fig. 6 for the equimolar composition. Clearly, the Neumann–Kopp rule (Eq. 1) is not the best way to evaluate C_P of the liquid solution in this case. Since one would expect that the glass transition temperature for the solution is somewhere below the liquidus temperature, a better estimate would be to extrapolate the constant heat capacities of pure liquid A and B from their melting temperatures down to T_g of the solution. Below this temperature, C_P of the solution in the glass state can be evaluated using the Neumann–Kopp rule from the heat capacities of pure solid A and B. C_P of the equimolar composition obtained in such a way is shown in Fig. 6 by the dashed lines, assuming that T_g = 1100 K for this composition. The A–B phase diagram calculated using the latter way of estimating C_P is shown by the dashed lines in Fig. 5.

Several conclusions can be drawn from this simple example. The effect of evaluating C_P of the solution using the two different methods shown in Fig. 6 is substantial. Even though the difference in the enthalpy at 1100 K is not very large, just 6.7 kJ mol^{-1}, the difference in the calculated eutectic temperature is 65 K. Furthermore, let us assume that the dashed lines in Figs. 5 and 6 correspond to the reality that one would like to reproduce with a thermodynamic model. It would be difficult to do so starting from the standard CALPHAD approach of estimating C_P of the solution from the heat capacities of pure liquid A and B by the Neumann–Kopp rule and trying to compensate the inaccuracy in C_P with excess parameters. One would have to introduce the excess heat capacity which is not only composition-dependent, but also becomes zero above 1900 K and below 1100 K. This cannot be done using the standard functions that are currently available for excess C_P in all thermodynamic software packages.

One way of dealing with this problem is to use pure components of the liquid solution that are not the real pure A and B liquids with their glass transition temperatures, but rather hypothetical pure liquids that are obtained by extrapolation of C_P down from the melting temperature without a drop at the corresponding T_g. The phase diagram and the thermodynamic properties above the liquidus should then be correct, but the liquid solution cannot be used to calculate the properties of glass. Furthermore, care must be taken to ensure that liquid does not become more stable than the corresponding solid phase at low temperature.

A better and more general way would be to estimate T_g of a liquid solution as a function of composition and to take it directly into account in calculating C_P of the solution like it was done for the dashed lines in Fig. 6. The liquid and the glass state will then be described by the same solution. For example T_g can be calculated by a separate viscosity database, or it can be estimated and stored in the structure of the thermodynamic database like the Curie temperature is stored for magnetic solutions. Of course in the latter case, one still has to develop a reasonable method of estimating the composition dependence of T_g for multi-component solutions.

5 CALPHAD models for liquids

5.1 Single-state models The CALPHAD liquid models currently used, and various others that have been proposed, are all functions describing the temperature dependence of the properties of the average atom in the liquid phase. These functions are generally polynomials such as those used by SGTE [1] or the Shomate equation [57] used by the NIST Chemistry Webbook [58]. Unlike SGTE, where the functions cover the temperature range from 298 to 6000 K, the Shomate equations from the NIST Chemistry Webbook are only valid above the melting point. To cover the large temperature range, SGTE accepted discontinuities in the heat capacities that were described in Section 1. Models other than polynomial descriptions have rarely been used for liquids. We are not aware that descriptions based on Einstein or Debye models have been used for describing liquids over the large temperature ranges that are customary for the CALPHAD method. Agren et al. [2] tested a description based on Hoch's [59] series expansion of the Debye function. In order to extrapolate the liquid below the Kauzmann temperature and the solid above the 'inverse' Kauzmann temperature ($\boldsymbol{S}^{\mathrm{sol}} > \boldsymbol{S}^{\mathrm{L}}$), discontinuities were introduced to the respective heat capacities of the solid and liquid. To summarize, the functions used in these single-state formalisms are either limited in the temperature range that can be covered or suffer from discontinuities in the heat capacities.

5.2 Two-state model The physical picture of atoms gradually changing from vibrational degrees of freedom (solid-like behaviour at lower temperatures) to translational degrees of freedom (liquid-like behaviour at higher temperatures) is the basis for the two-state model. This can be compared with the 'free-volume' model [31] where the liquid at high temperature is assumed to have a higher fraction of free volume than at lower temperature. The formalism suggested by the two-state model allows a description of undercooled liquid and amorphous phases in multi-component systems. It overcomes some limitations due to the SGTE description of undercooled liquids (e.g. kink in $\boldsymbol{C}_{\mathrm{P}}$ at the $\boldsymbol{T}_{\mathrm{M}}$ of pure components [62]). The two-state model has already been applied to describe pure components such as Sn, Cu [2], and Fe [60]. The multi-component version of the two-state model was first demonstrated for the Ag–Cu system [61] and later for the Fe–B system [62]. A full assessment of the Au–Si system based on the two-state model has recently been developed [63].

This approach seems consistent with understanding of glassy behaviour derived from experiment and molecular simulation (caged vs. free atoms), though it does not capture the full complexity of an energy landscape approach. However, the relative simplicity of the model without ignoring the characteristic features of the liquid suggests that it is a reasonable approach to modelling liquids and amorphous phases in the CALPHAD approach.

In the two-state model [2, 4], the constituents in the liquid are thus assumed to be either in a solid-like or a liquid-like state. The difference in Gibbs energy between the two states is given by

$$\Delta G_{\mathrm{m}}^{\mathrm{d}} = G_{\mathrm{m}}^{\mathrm{liq}} - G_{\mathrm{m}}^{\mathrm{sol}} = H_{\mathrm{m}}^{\mathrm{liq}} - H_{\mathrm{m}}^{\mathrm{sol}} - RT + \cdots, \qquad (2)$$

where the entropy difference $\boldsymbol{R}$, equal to the gas constant, is the so-called communal entropy [64]. 'm' denotes molar quantities, and 'sol' refers to atoms without translational degrees of freedom. Higher order terms may be added as indicated by the data. Since there is a gradual transition at each temperature, a certain fraction of the atoms, χ, are liquid-like and the fraction $1 - \chi$ are solid-like. Assuming a random mixture of the two states the Gibbs energy of a liquid is

$$G_{\mathrm{m}}^{\mathrm{L}} = G_{\mathrm{m}}^{\mathrm{sol}} + \chi \Delta G_{\mathrm{m}}^{\mathrm{d}} + RT((1-\chi)\ln(1-\chi) + \chi \ln \chi). \qquad (3)$$

The variable χ is an internal order parameter and at equilibrium it has the value that minimizes the Gibbs energy. From the condition $\partial \boldsymbol{G}^{\mathrm{L}}{}_{\mathrm{m}}/\partial\chi = 0$, we obtain the equilibrium value of χ,

$$\chi = \frac{\exp(-\Delta G_{\mathrm{m}}^{\mathrm{d}}/RT)}{1 + \exp(-\Delta G_{\mathrm{m}}^{\mathrm{d}}/RT)}. \qquad (4)$$

By inserting Eq. (4) in Eq. (3) we thus obtain for a liquid in internal equilibrium

$$G_m^L = G_m^{sol} - RT \ln\left(1 + \exp\left(\frac{-\Delta G_m^d}{RT}\right)\right). \quad (5)$$

The entropy is obtained as $-\mathrm{d}\boldsymbol{G}_m^{\,L}/\mathrm{d}\boldsymbol{T}$. Thus

$$S_m^L = S_m^{sol} - \chi\frac{\mathrm{d}\Delta G_m^d}{\mathrm{d}T} - R((1-\chi)\ln(1-\chi) + \chi\ln\chi), \quad (6)$$

where $\boldsymbol{S}_m^{\,sol} = -\mathrm{d}\boldsymbol{G}^{sol}{}_m/\mathrm{d}\boldsymbol{T}$ and the derivative $\mathrm{d}\boldsymbol{G}_m/\mathrm{d}\boldsymbol{\chi} = 0$ in view of the equilibrium condition. The enthalpy is

$$H_m^L = H_m^{sol} + \chi\Delta H_m^d, \quad (7)$$

where $\boldsymbol{H}_m^{\,sol} = -\boldsymbol{T}^{\,2}\mathrm{d}(\boldsymbol{G}^{sol}{}_m/\boldsymbol{T})/\mathrm{d}\boldsymbol{T}$ and $\boldsymbol{H}_m^{\,d} = -\boldsymbol{T}^{\,2}\mathrm{d}(\boldsymbol{G}^{d}{}_m/\boldsymbol{T})/\mathrm{d}\boldsymbol{T}$. For the heat capacity one obtains

$$C_p^L = C_p^{sol} + \chi\frac{\mathrm{d}\Delta H_m^d}{\mathrm{d}T} + \Delta H_m^d\frac{\mathrm{d}\chi}{\mathrm{d}T}, \quad (8)$$

where $\boldsymbol{C}_P^{\,sol} = -\boldsymbol{T}\,\mathrm{d}^2\boldsymbol{G}^{sol}{}_m/\mathrm{d}\boldsymbol{T}^{\,2}$. The derivative $\mathrm{d}\boldsymbol{\chi}/\mathrm{d}\boldsymbol{T}$ is then obtained as

$$\frac{\mathrm{d}\chi}{\mathrm{d}T} = \frac{\Delta H_m^d}{RT^2}\frac{\exp(-\Delta G_m^d/RT)}{(1+\exp(-\Delta G_m^d/RT))^2}. \quad (9)$$

The final expression for the heat capacity is obtained by inserting Eq. (9) in Eq. (8):

$$C_p^L = C_p^{sol} + \chi\frac{\mathrm{d}\Delta H_m^d}{\mathrm{d}T} + R\left(\frac{\Delta H_m^d}{RT}\right)^2 \times \frac{\exp(-\Delta G_m^d/RT)}{(1+\exp(-\Delta G_m^d/RT))^2}. \quad (10)$$

It should be emphasized that Eqs. (3)–(10) are valid for any temperature dependence of Gmd .

We shall now turn to a discussion of how the parameters in the model may be evaluated from experimental information. The solid-like state should be regarded as a hypothetical ideal amorphous phase where all constituents have only vibrational degrees of freedom and can be described by a function like $\boldsymbol{G}^{sol}{}_m = \boldsymbol{G}^{cryst}{}_m + \boldsymbol{A} + \boldsymbol{dT}^{\,2}$. A somewhat naive approximation would be to regard it as having the same entropy and heat capacity as the stable crystalline structure but a higher energy. We would then take $\boldsymbol{G}^{sol}{}_m = \boldsymbol{G}^{cryst}{}_m + \boldsymbol{A}$, where $\boldsymbol{A}$ is an adjustable parameter. From the condition that the liquid and crystalline phase have the same Gibbs energy at the melting point, i.e. $\boldsymbol{G}^{cryst}{}_m = \boldsymbol{G}^{sol}{}_m - \boldsymbol{RT}\ln(1 + \exp(-\boldsymbol{G}^{d}{}_m/\boldsymbol{RT}))$ we obtain $\boldsymbol{A}$. The state when all con-stituents have translational degrees of freedom would have an even higher energy and also higher entropy. As a first approximation we would take $\boldsymbol{G}^{liq}{}_m = \boldsymbol{G}^{sol}{}_m + \boldsymbol{B} - \boldsymbol{RT}$, where we have taken the entropy difference as $\boldsymbol{R}$, the communal entropy. We thus obtain $\boldsymbol{G}^{d}{}_m = \boldsymbol{B} - \boldsymbol{RT}$ and therefore

$$A = RT\ln\left(1 + \exp - \left(\frac{(B - RT_M)}{RT_M}\right)\right). \quad (11)$$

Table 1 Two parameter approximation of the two-state model.

element	T_M (K)	H_M (J mol^{-1})	S_M (J mol^{-1} K^{-1})	A (J mol^{-1})	B (J mol^{-1})	$\chi(T_M)$
Al	933.47	10 711	11.4744	no solution		
Si	1687	50 208	29.7617	no solution		
Fe	1811	13 806	7.6241	5441.2	27581.7	0.30
Ni	1728.30	17479.82	10.1137	10681.5	12962.2	0.52
Cu	1358	13 263	9.7684	7430.04	12098.1	0.48
Zr	2127.85	20997.77	9.8681	12044.6	18131.8	0.49
W	3695	52313.69	14.1580	no solution		
Se	494	6694.6	13.5514	no solution		
Au	1337.33	12 552	9.3859	6404.26	13693.9	0.44
Sn	505.078	7027.12	13.9169	no solution		
Pb	600.612	4773.94	7.9485	1964.47	8638.42	0.33
Re	3459	60 428	17.4698	no solution		
Ag	1234.93	11296.8	9.1477	5592.15	13584.3	0.42

We thus have two adjustable parameters, A and B, and can fit two pieces of information exactly. We would probably like to fit the melting point for the stable crystalline phase TM and the enthalpy of melting HM. The difference in enthalpy between liquid and the crystalline phase at the melting point given by the model is HM = A + χB and, combined with Eqs. (11) and (4), we have two nonlinear equations to calculate A and B.

The above approximation is a convenient way to determine the parameters if no heat capacity data are available for the liquid phase or to determine the start values for more complex descriptions. This approximation was tested for a number of elements and, as can be seen in Table 1, it was found that for roughly half of the cases no solution exists for the two nonlinear equations. For most of the elements where solutions were found, approximately half of the atoms are in the vibrational state. In the case of Cu, the heat capacity of the liquid becomes 2 J mol^{-1} K^{-1} larger than that of the crystal. The SGTE database gives half that value whereas the more recent values of Wilde [15] give 1.6 J mol^{-1} K^{-1}. It is interesting to note that the ideal amorphous phase has an enthalpy that is approximately half the heat of melting higher than that of the crystal. It may be worthwhile noting that, for all elements for which no solution was found, the entropy of melting is larger than ≈11 J mol^{-1} K^{-1} or ≈1.25$\boldsymbol{R}$. If this approximation is applied to compounds, care must be taken to account for the number of atoms in the equations.

If one wants to represent the heat capacity of the liquid at the melting point, one more adjustable parameter may be needed. For example one may choose to allow the ideal amorphous phase to have a slightly different heat capacity from that of the stable crystalline structure or optimize the entropy difference between the liquid-like state and the solid-like state. If heat capacity data are available over an extended temperature range for liquid and/or amorphous phases, more general representations are most likely needed for the Gibbs energies of the ideal amorphous phase and the two-state difference [2, 60–62].

The application of the two-state model has already been shown for Sn, Cu [2] and Fe [60]. In all cases, the trend for the heat capacity to increase upon undercooling has been captured. In the case of Fe [60], the two-state model gave a crystallization enthalpy for amorphous Fe in good agreement with both direct and indirect experimental data, while it is simply impossible for the SGTE data to do so. Here one more test has been given for Au, of which the heat capacity data are available both well above and below its melting point [15].

In order to fit the liquid heat capacity data for Au, a good description of the crystalline phase is needed first. Assuming the ideal amorphous phase has the same harmonic vibration, we may write the Gibbs energy of the ideal amorphous phase using the Einstein model as $\boldsymbol{G}^{\mathrm{sol}}_{\mathrm{m}} = \boldsymbol{G}^{\boldsymbol{h}}_{\mathrm{m}}(\boldsymbol{\theta}_{\mathrm{E}}^{\mathrm{fcc}}/\boldsymbol{T}) + \boldsymbol{A} + \boldsymbol{dT}^{2}$, where the Einstein temperature, $\boldsymbol{\theta}_{\mathrm{E}}^{\mathrm{fcc}}$, is obtained as 125.82 K for Au by using the same approach adopted for Fe [60]. If just $\boldsymbol{T}_{\mathrm{M}}$, $\boldsymbol{H}_{\mathrm{M}}$, and $\boldsymbol{C}_{\mathrm{P}}^{\mathrm{L}}(\boldsymbol{T}_{\mathrm{M}})$ values are used for the two-state model, only one parameter is available to describe the Gibbs energy difference of the two states. Following the suggestion that $\boldsymbol{G}^{\mathrm{d}}_{\mathrm{m}} = \boldsymbol{B} - \boldsymbol{RT}$, and using an optimization procedure, the following results are obtained: $\boldsymbol{A} = -1041.203$ J mol^{-1}, $\boldsymbol{d} = -1.713954 \times 10^{-3}$ J mol^{-1} K^{-2}, $\boldsymbol{B} = 14280.62$ J mol^{-1}.

The calculated heat capacity for Au is depicted in Fig. 7. The present result is already in surprisingly good agreement with the measurements. Further testing with inclusion of more heat capacity data in an optimization with additional parameters shows only a very tiny modification to the communal entropy used for $\boldsymbol{G}^{\mathrm{d}}_{\mathrm{m}}$. This means no more parameters are needed in this fortuitous case. In other cases, a general form as suggested in Ref. [2] may be required.

It is worth mentioning that one may be tempted to use directly the data on the heat capacity difference between liquid and crystalline solid phases to fit $\boldsymbol{C}_{\mathrm{P}} = \boldsymbol{C}_{\mathrm{P}}^{\mathrm{L}} - \boldsymbol{C}_{\mathrm{P}}^{\mathrm{sol}}$ according to Eq. (8). This is not appropriate because $\boldsymbol{C}_{\mathrm{P}}^{\mathrm{sol}}$ is the heat capacity of the ideal amorphous phase, which is not necessarily the same as that of the crystalline phase, and most importantly the uncertainty or error of $\boldsymbol{C}_{\mathrm{P}}$ could be huge since it contains not only that of $\boldsymbol{C}_{\mathrm{P}}^{\mathrm{L}}$ but also that of $\boldsymbol{C}_{\mathrm{P}}^{\mathrm{cryst}}$, especially in the vicinity of the melting point. Therefore, it is important to always follow the steps described above in the case study for Au.

Another test of the two-state model was done for Ga where heat capacity data were available both well above and below the melting temperature (302.91 K). The solid orthorhombic phase was first evaluated using these data and $\boldsymbol{\theta}_{\mathrm{E}}^{\mathrm{ortho}}$ was evaluated to 188 K. Using a corresponding equation for $\boldsymbol{G}^{\mathrm{sol}}_{\mathrm{m}}$ as the one used for Au, the parameters $\boldsymbol{A}$ and $\boldsymbol{d}$ and the difference in Gibbs energy between the solid-like and the liquid-like states, $\boldsymbol{G}^{\mathrm{d}}_{\mathrm{m}} = \boldsymbol{B} + \boldsymbol{bT}$, were evaluated using the melting temperature, $\boldsymbol{T}_{\mathrm{M}}$, the melting enthalpy, $\boldsymbol{H}_{\mathrm{M}}$, and the heat capacity for the liquid at the melting temperature, $\boldsymbol{C}_{\mathrm{P}}^{\mathrm{L}}(\boldsymbol{T}_{\mathrm{M}})$. However, instead of making $\boldsymbol{b}$ equal to the communal entropy it was fixed to the melting entropy as suggested in Ref. [60]. According to the SGTE compilation [1], the melting entropy of Ga is 18.4535 J mol^{-1} K^{-1}, much higher than the communal entropy.

Using an optimization procedure, the following values were obtained: $\boldsymbol{A} = -4595$ J mol^{-1}, $\boldsymbol{d} = -0.002376$ J^{-1} K^{-2} K^{-1} and $\boldsymbol{B} = 3174$ J mol^{-1} K^{-1}and, as already mentioned, $\boldsymbol{b}$ was fixed to −18.4535 J mol^{-1} K^{-1}. The calculated heat capacity is shown in Fig. 8 compared to experimental data from Takahashi et al. [11]. The heat capacity data were used to evaluate the description of the solid phase but only used as a comparison for the liquid and undercooled liquid.

To improve the results the entropy term, $\boldsymbol{b}$ in $\boldsymbol{G}^{d}_{m}$ was optimized and the heat capacity at a high temperature was added as experimental information. The result can be seen in Fig. 9 ($\boldsymbol{A}$ = − 4782 J mol^{-1} , $\boldsymbol{d}$ = 1 1 0.0008893 J mol^{-1} K^{-2}, $\boldsymbol{B}$ = 3651 J mol^{-} 1 and $\boldsymbol{b}$ = −19.7942 J mol^{-} K^{-}). The entropy term changed slightly from the entropy of melting

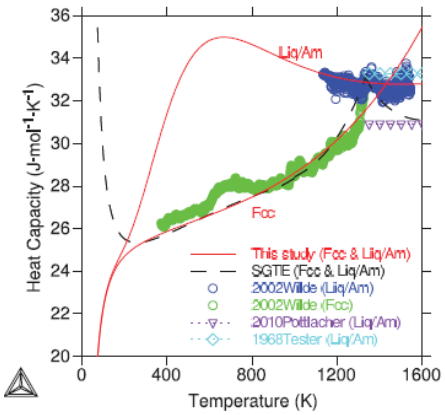

Figure 7 Comparison of the results on the heat capacity of Au from the two-state model in this study, SGTE [1], and experiments [15, 65, 66].

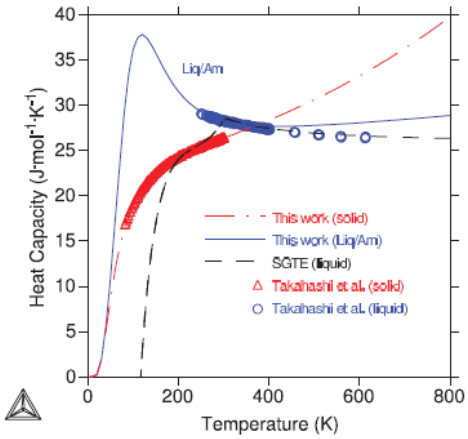

Figure 8 The heat capacity of solid and liquid Ga. Three parameters were optimized for the liquid to fit the melting temperature, the heat of melting and the heat capacity of the liquid at the melting temperature. The entropy term $\boldsymbol{G}^{d}_{m}$ was fixed to the value of the entropy of melting as given by SGTE. The result is compared to experimental data [11].

and the result above the melting temperature was improved. To improve the result, more heat capacity data could be included and more terms added.

These two examples demonstrate that the quality of the description of the liquid is strongly tied to the quality of the description of the solid-like atoms. Therefore, approximations such as using the two parameter approximation or a heat capacity for the solid-like atoms that is identical to that of the crystalline phase should only be used if insufficient data for the evaluation of the parameters are available. If insufficient data are available from experiments, data from computational predictions should be sought out.

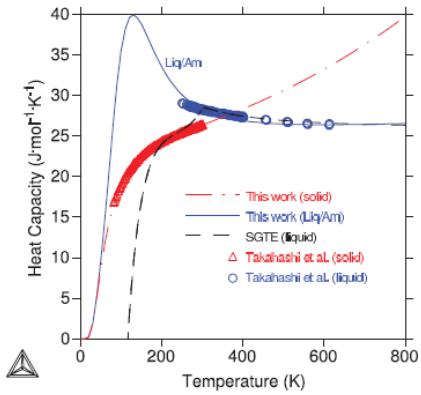

Figure 9 The heat capacity of solid and liquid Ga as in Fig. 8 but here the entropy term was allowed to vary and an additional high temperature C_P point was added as experimental input.

We now turn to the representation of kinetic properties and will discuss the viscosity. The experimental information indicate, see, for example [67], non-Arrhenius behaviour at higher temperatures whereas it indicates Arrhenius behaviour in the glassy state. The kinetics of undercooled liquids had been modelled earlier by the free-volume approach [68] and for the self diffusion, D, an expression of the form below was suggested

$$D = D_0 \exp\left(\frac{-f_1}{f_V(T)}\right), \qquad (12)$$

where D_0 and f_1 are properties of the liquid related to the activation energy and geometric environment of the atoms, respectively, and $f_V(T)$ is the fraction of free volume. Using the two-state model we would replace f_1/f_V with f_χ/χ. χ is then calculated from Eq. (4) for the equilibrium liquid and set constant for a glass. Allowing for Arrhenius behaviour in glassy state, it seems natural to suggest the following expressions for the full temperature range covering high-temperature and undercooled liquid as well as the glassy state.

$$D = D_0 \exp\left(\frac{-Q(1-\chi)}{RT}\right) \exp\left(\frac{-f_\chi}{\chi}\right), \qquad (13)$$

For the viscosity η we would then write

$$\eta = C \exp\left(\frac{Q(1-\chi)}{RT}\right) \exp\left(\frac{f_\chi}{\chi}\right), \qquad (14)$$

where Q, C and f_χ are material properties. The activation energy in the glassy state then is $Q(1-\chi)$, i.e. the more liquid-like atoms the frozen-in structure has, the lower the activation energy is. Equations (13) and (14) then cover the whole temperature range. However, in the glassy state χ is constant. Once the parameters in Eq. (14) have been deter-mined one may calculate the glass temperature T_g as the temperature where $\eta = 10^{12}$ Pa s.

6 Contributions from atomic-scale methods

6.1 Methods and approximations Many previous models of liquids, e.g. in CALPHAD modelling, primarily utilized experimental data, but there is growing use of theoretical methods for input and validation, particularly where little or no experimental data exist. Atomic-scale (so-called quantum-mechanical/first-principles/*ab initio* and classi-cal/empirical) methods can be used to understand phenomena and mechanisms in addition to providing data. They are all based on calculating energies and forces between atoms and summing over the individual contributions to get the proper-ties of the whole. Generally, increased physical fidelity comes at the price of calculation speed, and thus system size.

Most fundamental (and most theoretically rigorous) are the first-principles, or *ab initio*, methods that explicitly model interatomic interactions from direct calculations of the electron density within the framework of electronic

density-functional theory (DFT). These methods, however, are limited in size, typically to fewer than a thousand atoms, due to calculation expense. (Ref. [69] has a treatment of uncertainties associated with DFT for crystalline elements.) There are various examples of first-principles-based simulations of liquids, e.g. in Refs. [20, 70–73], but a comprehensive review is outside the scope of this paper.

A less theoretically rigorous, but faster, approach is the semi-empirical tight-binding method (TBM) [74, 75], which arises from further approximations to the quantum-mechanical description of the interatomic interactions. The fastest, but most approximate, treatment of energies comes from interatomic potentials (also called force fields). In this method, a functional form is postulated and then data (experimental or from first-principles) are used to parameterize the functions that describe the energies and forces of interacting atoms. Some of these functions are rather simple, while others are complicated and thus relatively costly to calculate. As will be discussed in more detail, the interatomic potential that is used (along with other simulation choices) can strongly influence the simulation results, and a poor choice of interatomic potential can undermine an otherwise good calculation. This is important to recognize when considering the results from these simulations.

Once the energetic descriptions are chosen, they can be used as part of an atomic-scale, or atomistic, simulation approach. Most common in liquids are the MD or Monte-Carlo (MC) methods. These are described in many references, including [76]. When the forces at each time step in MD are determined using DFT methods, the simulation method is called '*ab initio* MD' or AIMD [70, 71]. When interatomic potentials are used, it is called 'classical MD' or just MD. Classical MD is currently the atomistic method that allows the times and system sizes needed for many liquid kinetic processes, as well as phase transitions between liquids and various solid phases. Additionally, classical MD and Monte-Carlo methods allow studies of thermodynamics and defects of larger systems (up to billions of atoms), such as those including grain boundaries or solid-liquid interfaces. Here, we limit ourselves to simulations related to single-phase, elemental liquids, though alloys and mixtures are commonly studied.

There are some issues associated with the use of classical atomistic simulation methods. A major one is the dependence of simulation answers on the interatomic potential. This is addressed extensively in Ref. [77], among others. Additionally, to compare MD enthalpies and heat capacities with experiment, the electronic heat capacity should be added [7] as well as the magnetic contributions in spin-polarized systems. Another issue particularly relevant for CALPHAD modelling is the choice of reference state when reporting energies. MD results are often presented as reported by the simulation software (in absolute units such as eV/atom). Much less common is for the energy to be reported with respect to a reference state such as a fcc crystal at 300 K. Ambiguous reference states makes comparison of thermo-dynamic quantities, such as enthalpy, much more difficult.

Coupled classical and *ab initio* MD provide a productive avenue for liquid modelling that will likely become more common. This approach uses the speed of classical MD with the quantum-mechanical treatment of a first-principles calculation, e.g. in Ref. [72]. For example a liquid could be equilibrated using classical MD followed by a DFT calculation that would otherwise be too expensive to be feasible.

6.2 Molecular dynamics example: Au and Ni We performed MD simulations to demonstrate the type of information that can be obtained from atomistic simulations and some of the subtleties that must be considered when using the results. Specifically we wanted to highlight the effect of the interatomic potential choice and some of the topics mentioned above related to reference states and making comparisons with experimental results. It is important to note here that we are not making recommendations on which inter-atomic potentials are 'the best'. That depends on what is being studied. Ideally, a single interatomic potential would be the best at capturing every material property related to crystals, liquids, surfaces, interfaces, defects, etc. In reality, most interatomic potentials are heavily optimized for one type of simulation (e.g. crystalline solids) and may not work well for others, or they are optimized to reproduce a range of properties reasonably well at the expense of the accuracy for a single one. The researcher using the potentials must make selections based on how well they reproduce the materials properties relevant for the problem under consideration, and no single interatomic potential will be the best choice for all problems.

For this work, we selected four interatomic potentials – two for Au and two for Ni. This is a small subset of the available interatomic potentials for these elements because our intention was to use them as an example. Additional simulations need to be done to provide comprehensive assessments. These interatomic potentials were of the of the embedded atom method (EAM) [78–80] or Finnis–Sinclair [81] forms that are commonly used to simulate metals, and they are non-magnetic. They are all available from the NIST Interatomic Potentials Repository [77]. Some issues related to the selection and use of interatomic potentials (also known as force fields) are also addressed in detail in Ref. [77]. Here the Au potentials were denoted as Au-G05 (Ref. [82]) and Au-A87 (Ref. [83]). The Au-A87 potential was fit using crystalline properties and optimized for treating crystalline Au, including defects [83]. Au-G05 included fitting information from an AIMD simulation of liquid Au as well as information from the radial distribution functions for liquid Au. The reported melting temperature for Au-G05 is 1159 K, 13% lower than the experimental value of 1337 K, in part due to the difficulties of simultaneously optimizing for both surface properties and liquid density [82].

The Ni potentials were Ni-M09 (Ref. [84]) and Ni-M12 (Ref. [85]). The Ni-M09 potential (originally from Ref. [86]), used a number of 0 K solid properties (including bulk phases and defects) in the fit. Despite not fitting any finite temperature or liquid data, and not fitting to the melting temperature itself, the melting temperature of this potential is 1701 K (1.6% lower than the experimental melting temperature of 1728 K) [84]. The Ni-M12 potential was fit as part of an inter-atomic potential for liquid and amorphous $NiZr_2$. It included liquid AIMD simulations and X-ray diffraction data as part of the fitting process, and the properties of liquid Ni were a high priority during the optimization. The reported melting temperature is 1728 K [85].

Ideal, fully periodic, face-centred cubic (fcc) crystals of 4000 atoms were heated using the LAMMPS molecular dynamics software package [87] from 1 to 2500 K in increments of 100 K, after which they were cooled again to 100 K using the same temperature intervals. At each temperature, both during heating and cooling, there was a period of equilibration followed by a so-called 'production' simulation, the data from which were used to determine the average thermodynamic quantities and structure. Additionally, for one interatomic potential at several temperatures, the simulations were allowed to run for additional steps to make sure that an observed low-temperature amorphous phase was not stable, but was instead the result of a very rapid cooling rate. This will be referenced as an 'extended' simulation. Energy, pressure, volume and structure were monitored for fixed temperature and with simulation volume allowed to change to minimize pressure (NPT ensemble). For the equilibrated simulations, since pressures were zero on average (within standard deviations at each temperature), the total energy (potential and kinetic) was the enthalpy. Enthalpy, diffusion coefficients, local structure and order, and heat capacities were then examined. Additional simulation details are in Appendix B. Due to the small size of these simulations and the first-order nature of solidification to fcc, it is possible to achieve significant undercooling in these liquids. We note here that there are no known experimental bulk elemental glasses for Au or Ni formed from the liquid. We also note that these simulations are equivalent to a very high quench rate, and this is a known difficulty in comparing MD simulation results with experiments, as discussed in references such as Ref. [33].

Enthalpies were calculated for temperatures in 100 K increments for both the heating and cooling runs, but only the cooling enthalpies (referenced to fcc at 300 K) are given in Fig. 10. These show temperatures between 500 and 2500 K for all four interatomic potentials. It is important to emphasize here that the solidification temperatures discussed in this work are not the equilibrium melting temperatures for these interatomic potentials. Rather, these are the solidification temperatures that reflect undercooling possible due in part to the finite size of the system. For Au (top), the Au-G05

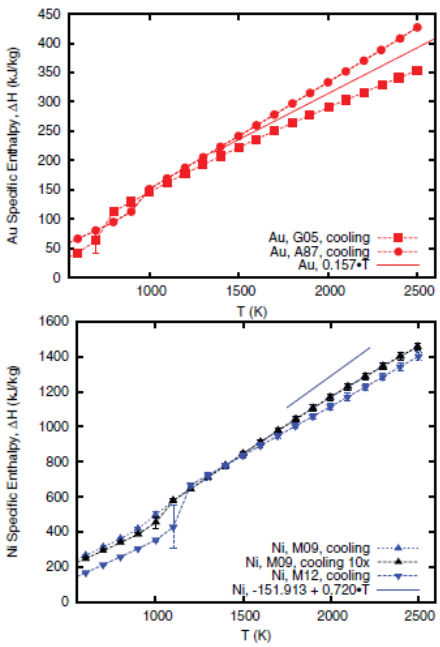

Figure 10 Enthalpies (***H*** , referenced to fcc at 300 K) during cooling of Au (top) and Ni (bottom). The kinks represent solidifica-tion to a crystalline or amorphous state as described in the text. The solid lines are experimental values from Ref. [65]. Lines connecting points are to guide the eye.

interatomic potential gives solidification between 700 and 800 K, as indicated by a kink in the enthalpy. Solidification happens between 900 and 1000 K for the Au-A87 potential. Ni (bottom) displayed more complicated behaviour. For the Ni-M12 interatomic potential, the kink in the enthalpy curve occurs between 1100 and 1200 K, with the large error bar at 1100 K indicating that solidification (crystallization) actually occurred during the simulation. For Ni-M09, the cooling runs yielded a low-temperature amorphous structure with enthalpies dependent on cooling rate (standard production run, and one where the cooling was an order of magnitude slower) as indicated by the divergence of the Ni-M09 curves. The decrease in enthalpy with solidification was not nearly as substantial as for the other potentials. For this potential, the extended run yielded a crystalline structure at 1000 K, indicating that the amorphous phase is not the stable one, even if it persists to low temperature due to the high cooling rate. The lines (without points) are experimentally determined enthalpies [65]. In Fig. 10, the electronic heat capacity contributions ($\gamma T^2/2$) have not been added to the enthalpy because the temperature range covers both solid and liquid phases.

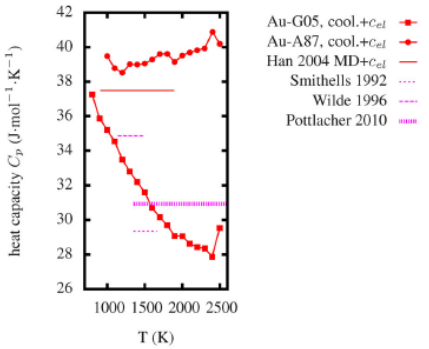

Figure 11 Liquid heat capacities C_P for Au from molecular dynamics. Previous simulations and experimental results are given for comparison. References are given in the text.

Heat capacities for the liquids are given in Figs. 11 and 12, along with MD results from the literature [17, 18]. The current results were determined by taking numerical derivatives of the liquid enthalpies with respect to temperature for zero-pressure (on average) simulations. In this work, we are estimating the electronic heat capacity contribution from electronic density of state calculations of the liquids. For Au, this was done from a set of tight-binding MD simulations [90], while for Ni it was based on an AIMD calculation [73]. This method uses the relationship $c_{el} = (\pi^2/3)k_B^2 T \cdot 2N(E_F)$ where $2N(E_F)$ is the DoS at the Fermi level and T is the temperature. This approximation gives values of 3.2 J mol^{-1} K^{-1} for Au at 1773 K and 11.2 J mol^{-1} K^{-1} for Ni at 1900 K. These are added to the MD values as constants since we do not know the temperature dependence of $N(E_F)$. We note that the difference in magnitude of these corrections is significantly larger for Ni than Au.

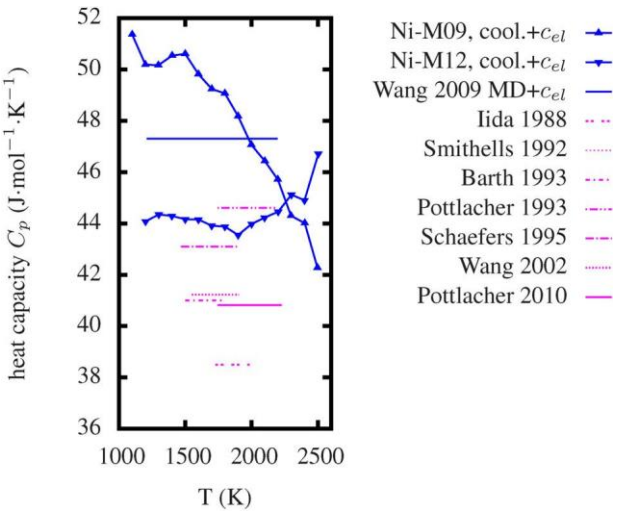

Figure 12 Liquid heat capacities C_P for Ni from molecular dynamics. Previous simulations and experimental results are given for comparison. References are given in the text.

From Figs. 11 and 12, it can be seen that heat capacities for Au-A87 and Ni-M12 are approximately flat with values of 36 and 33–34 J mol^{-1} K^{-1}, respectively. Au-G05 and Ni-M09 increase with decreasing temperature, by as much as 30%. These data do not show significantly different heat capacity behaviour for liquids above the melting temperature versus for undercooled liquids for any of the potentials. From these results, it can again be seen that behaviour in molecular dynamics simulations can depend on interatomic potential. However, the ranges are generally consistent with experiments [91–96]. From Figs. 11 and 12, it is interesting to note that, while individual experimental measurements of the heat capacity are constant with temperature (dotted lines), they show a trend of decreased heat capacity with increasing temperature for Au but not for Ni (though the experimental data for Au are more limited). It is also interesting to compare Fig. 11 with Fig. 7 and the representation of the experimental data by the two-state model. As can be seen the results from the potential Au-G05 and the two-state model are in good agreement. In these simulations, Au-G05 and Ni-M12 appear to be more consistent with the heat capacity experiments (including the experimental values in Fig. 7) than Au-A87 and Ni-M09. This is consistent with the fitting choices made for the potentials. More work is needed to assess which interatomic potentials would give the most accurate liquid heat capacity results and which reference data to use in making that determination.

To help understand the enthalpy and heat capacity results, we will examine selected snapshots of atomic coordinates from the MD simulations. These snapshots represent instantaneous atomic configurations that can be used to look for crystallinity, local environment, the presence of defects such as grain boundaries, etc. Examples are shown in Fig. 13 for the Ni-M09 interatomic potential. Figure 13a shows Ni at 1100 K at the end of a production run of 300 000 steps, which also corresponds to the start of an extended run. The structure is amorphous with atoms coloured by the local environment determined by common neighbour analysis (CNA) [88]. In these snapshots, green represents atoms in a local fcc environment, red corresponds to hcp, cyan is icosahedral, and grey corresponds to ‘other’, meaning no identified structure. No bcc atoms were identified in these snapshots. After an additional 2 000 000 steps of an extended run, the structure is still amorphous with isolated cyan atoms indicating local icosahedral ordering (Fig. 13b). The case is different at 1000 K, where crystallization happens during the extended run. Figure 13c shows the final snapshot of the regular production run (first snapshot of the extended run), while Fig. 13d shows that the fcc crystal is more stable than the amorphous (glassy) phase at 1000 K. In this case, the simulation crystallized into two fcc crystallites with grain boundaries between them due to the fully periodic boundary conditions. Examination of the local structure helps understand amorphous versus crystalline behaviour, but it does not answer whether the Ni-M09 structure at the start of the extended run (Fig. 13c) is a liquid or solid at 1000 K.

a) Ni-M09 at 1100 K initial snapshot of extended run.

b) Ni-M09 at 1100 K final snapshot of extended run.

c) Ni-M09 at 1000 K initial snapshot of extended run.

d) Ni-M09 at 1000 K final snapshot of extended run.

Figure 13 Snapshots of the extended simulations (additional 2 million steps) at 1100 and 1000 K to examine stability of the amorphous phases. At 1100 K, the simulation remained in an amorphous state, while at 1000 K crystallization occurred leaving two fcc slabs with crystalline defects and a grain boundary between them. Green atoms represent local fcc environments, red corresponds to hcp, cyan is icosahedral, and grey is 'other' (no recognized structure).

To help determine the nature of the Ni-M09 amorphous phase at 1000 K, we also looked at the diffusion coefficient.

In this work, the relation $\boldsymbol{D} = {}_{r}2\ \ 2$ was used, where $/6\boldsymbol{t}\ \ \boldsymbol{D}$ is the self diffusion coefficient, **r** is the mean square displacement of the atoms, **r** is the instantaneous displacement of each atom relative to its initial position, and ***t*** is the elapsed time. ***D*** was calculated with atomic coordinates from the first and last snapshots of the production run in order to confirm liquid versus glassy atomic motion. A very small value of the diffusion coefficient ($\boldsymbol{D} = 5.3 \times 10^{-11}$ m^2s^{-1}) for Ni-M09 at 1000 K suggests a very viscous liquid or glass formed (at least temporarily) under this set of simulation conditions, even if the extended run later displayed that a crystalline state is more stable than the amorphous state. From examination of the local structure in Fig. 13c, there appear to be no nanograins, so grain boundary diffusion is highly unlikely. For reference, the calculated value of ***D*** at 1100 K was 2.4×10^{-10} m^2s^{-1}. For Ni-M12 at 1000 K (fcc with crystalline defects), $\boldsymbol{D} = 2.6 \times 10^{-12}$ m^2s^{-1}.

Centrosymmetry (CS) parameters [89] are shown in Fig. 14 for the MD simulations both above and below their solidification temperatures. CS parameters reflect the deviation of atom locations from an ideal fcc crystal structure, and these values are normalized by the square of the lattice

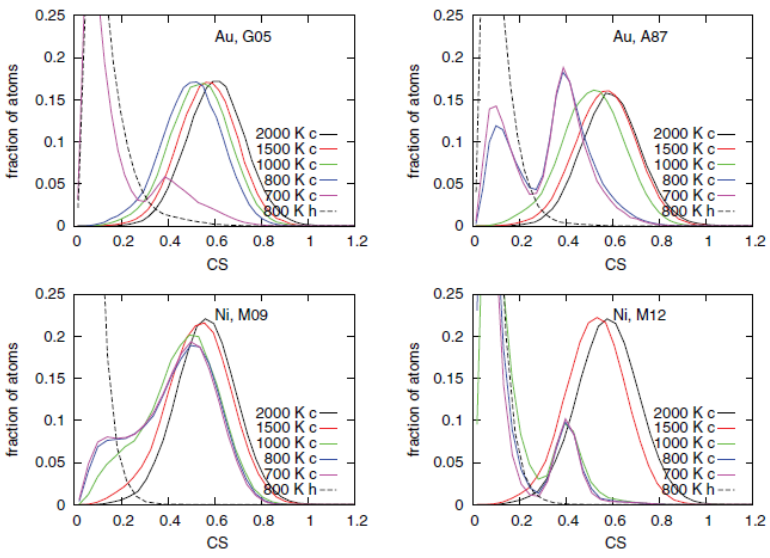

Figure 14 Centrosymmetry parameter from molecular dynamics for all potentials studied and a range of temperatures. See text for a description of the structure indicated by different values of the CS parameter. 'c' and 'h' denote cooling and heating simulations, respectively.

constant at the appropriate temperature. Thus peaks of 0–0.2 are seen for fcc, peaks near 0.4 appear for the hcp-type stacking faults that occur during solidification, and peak locations of approximately 0.5–0.6 are observed for liquids.

In Fig. 14, Au-G05 displays the same general behaviour as Au-A87 and Ni-M12, so we will describe it in detail. At 2000 K, there is a wide, broad peak centred around 0.6. This peak shifts down with decreasing temperature until solidification occurs and a strong peak appears near CS=0.1. The small peak at 0.4 comes from crystal defects. For reference, the profile of an fcc crystal at 800 K (heating run) is shown. The CS peak near 0.1 is broadened due to thermal effects. For Au-A87, the crystallized structure contains numerous grain boundaries, which accounts for the large peak at 0.4.

The Ni-M09 potential showed different behaviour during the cooling runs that started at 2500 K. The liquid peak shifted slightly to lower CS values with decreasing temperature, but near the 'solidification' transition, a distinct shoulder appears at lower CS values. This shoulder grows with decreasing temperature, but even at 100 K, the disorder is still observed in the production runs. Only after crystallization during the extended run at 1000 K is the distinct fcc peak seen. While the glassy behaviour of the Ni-M09 potential may be an artefact of the fitting optimizations, the centrosymmetry parameters for this phase display behaviour that deserves further study. The overlapping fcc and liquid CS distributions observed here tend to support a two-state type of approach where some atoms are in more solid-like environments while others are in more liquid-like local configurations. We again note, however, that an amorphous phase for Ni-M09 was not the most stable phase for this interatomic potential at low temperatures. It would be very interesting to examine centrosymmetry parameter distributions for well-characterized glass-forming systems.

More work needs to be done to fully characterize the liquid behaviour for these potentials and determine which are most appropriate for thermodynamic calculations of the type needed for CALPHAD modelling. Other properties such as density, viscosity, radial distribution function (or structure factor), latent heat, and volume changes on melting are all important in selecting an interatomic potential to use. Additionally, more work should be done to understand the corrections necessary to make meaningful comparisons with the experimental literature. This includes adequate treatment of the uncertainties associated with each method. Nevertheless, it seems that a possible approach to be used in practice could be to adjust the parameters of the CALPHAD two-state model to results from MD simulations in cases where experimental data are missing or conflicting.

7 Summary We began by outlining the issues with the SGTE database for the modelling of liquids in CALPHAD. We then gave an overview of the related experimental and theoretical understanding of liquids and glasses, followed by a detailed example and discussion related to B_2O_3. This was followed by an examination of the two-state model with several examples of fitted systems and a discussion of important issues in the use of this model. Of particular note is that the two-state formalism has the ability to describe relatively constant $\boldsymbol{C}_P$ at high temperatures as well as an increase of $\boldsymbol{C}_P$ with decreasing temperature below $\boldsymbol{T}_M$. We noted that two-state based models have been used in other modelling approaches for liquids. We finally described some of the issues with the use of first-principles calculations and molecular simulation in a CALPHAD framework.

The two-state model takes into account the changing degrees of freedom of the atoms in the liquid as temperature changes and, therefore, is in tune with the underlying physics. Although the two-state model shows great promise for CALPHAD type descriptions of the liquid phase more testing is required. Testing is especially needed to explore its suitability for liquids showing short range order. These liquids are described by special models, such as the ionic liquid sublattice model or modified quasi-chemical model, and may contain ionic and molecular species. Preferably testing should be carried out on a number of systems since it cannot be known in advance whether the properties of a specific system could reveal weaknesses of the two-state model.

Appendix A: Experimental methods that provide data on thermophysical properties With the development of tools and techniques for computer assisted calculations and simulations, knowledge of thermophysical properties at elevated temperatures up into the liquid phase became important. Thermophysical properties are defined in this paper as a selection of mechanical, electrical, optical and thermal material properties of metals and the thermal dependencies thereof, with a certain relevance to industrial, scientific and metallurgical applications (Table 2). This definition still covers a wide range of different material properties obtained by numerous different measurement techniques and approaches for the solid and the liquid phase.

According to the list of thermophysical properties mentioned before, some properties are of greater importance for use in industrial applications while others are of more scientific interest. The most relevant properties within this paper are melting temperature, heat of fusion and heat capacity used as input parameters for CALPHAD modelling.

A1. Ohmic pulse heating experiments A dynamic calorimetric pulse experiment utilizes resistive self-heating of an electrical conductor – typically wire shaped samples (with diameters ranging from some hundred micrometres up to a few millimetres), rectangular shaped samples (if the material cannot be drawn into wires and test samples have to be cut), foils, or tubes – by passing a large current pulse over the sample. As a result of the materials' resistivity the specimen can be heated from room temperature up to melting, further through the liquid phase and finally up to the boiling point within several microseconds. As these experiments are so fast, the liquid sample will not collapse due to gravitational forces, and also will not be able to interact with the ambient medium. Therefore, fast pulse heating also can be considered as a kind of 'containerless technique'.

Table 2 Thermophysical properties of solid and liquid metals, adapted from Ref. [97] and symbols proposed by IUPAC [118].

property	symbol	identifier
enthalpy	H	
heat of fusion	H_M	
isobaric/isochoric heat capacity	C_P /C_V	
density	d, ρ	
electrical resistivity	ρ	thermal and electrical properties that can also be obtained by means of ohmic pulse heating
thermal conductivity	λ, k	
thermal diffusivity	a	
phase transition temperatures	various	
melting temperature (pure metals)	T_M	
solidus/liquidus temperature (alloys)	T_s/ T_l	
critical pressure	P_c	
critical volume	V_c	critical parameters
critical temperature	T_C	
equation-of-state (EOS) parameters	various	EOS
speed of sound	c_s	
viscosity	η, μ	obtained by levitation techniques
surface tension	γ, σ	

The following components are common for all pulse heating experiments: energy storage (typically battery banks or capacitor banks) with charging unit, main switching unit (e.g., high-voltage mercury vapour ignition tubes), experimental chamber with windows for optical diagnostics and the ability to maintain a controlled ambient atmosphere. Pulse heating experiments are commonly performed under inert ambient atmosphere, e.g. nitrogen or argon at ambient pressure or in vacuum. Measurements can also be performed at ambient pressures up to 0.5 GPa under nearly isobaric conditions, the pressurized medium normally being argon or water. Quite often data recording equipment is placed in a shielded room.

Based on the initially measured quantities current, voltage drop, surface radiation and other optional optical measurements, several of the thermophysical properties listed in Table 2 can be deduced assuming that the mass or combination of density and volume of the sample at room temperature are known. For further very detailed reading see also Refs. [65, 97–99].

A2. Laser-pulse heating The main advantage of laser pulse heating is its use for the investigation of a broader variety of materials, such as metals, non-metals, ceramics and even fuel materials. Quite often this technique is used for investigating nuclear materials at very high temperatures. In a typical experiment, the sample is mounted inside an autoclave (or glove box) with controlled atmosphere. The energy is delivered to the sample in a localized way so that efficient heating results and small specimens can be used. The use of powerful ultra short laser pulses can result in very fast heating; thus extremely high temperatures may be achieved. The time regime covers the range of millisecond to femtosecond heating pulses. Thus, a large variety of different thermophysical properties can be analyzed for the liquid phase by means of laser pulse heating. Further reading is in Refs. [100, 101].

A3. Levitation experiments Containerless processing techniques provide non-contact conditions in which most interactions between the liquid sample and the environment are eliminated. In this method, the liquid sample is suspended or floated in a levitation cell by an external force. All that is required for levitation is a force vertically upwards equal to the object's weight. This can be accomplished by one of the following levitation techniques: electromagnetic levitation, aerodynamic levitation, acoustic levitation, electrostatic levitation or microgravity levitation such as parabolic flights or in space. Heating is done via induction from an AC power source (100 kHz to 1 MHz), an incandescent radiator or by laser radiation. Levitation techniques deal with high temperatures, mainly in the liquid range of the sample material. Levitation techniques are a good complementary technique to resistive pulse heating, as non-metallic samples can only be investigated by means of levitation. Moreover some thermophysical properties such as surface tension and viscosity can be obtained dynamically by means of levitation techniques.

For metallic melts, which are highly reactive, containerless processing by electromagnetic levitation is used quite often. Here the sample assumes a simple spherical shape, is contained in a clean environment, and can be studied over a large temperature range. Before starting an experiment the sample chamber must be evacuated; during the experiment the chamber is flushed with argon or helium. Electromagnetic levitators employ inhomogeneous radio-frequency electromagnetic fields to heat and position the samples. Such a field has two effects on a conducting, diamagnetic body. First, it induces eddy currents within the material, which, due to ohmic losses, eventually heats up the sample by inductive heating, and second, it exerts a Lorentz force on the body, pushing it towards regions of lower field strength. The latter effect can be used to compensate the gravitational force. By cooling the electromagnetic levitated sample with a cooling gas stream (Ar, He), undercooled liquid states can be obtained. See also Refs. [98, 99, 102, 103].

A4. Investigations with diamond anvil cells A diamond-anvil cell (DAC) generates a very high pressure (>100 GPa) by applying a moderate force to two diamond anvils. The diamonds are shaped such that there is a wide table face and a small culet face, which is on the order of 100 μm. Between the two culet faces of the diamonds is the gasket holding the sample. The basic principle of a DAC is that a force applied over a small area (here the culet face) results in a high stress. The stress in the sample is made hydro-static by surrounding it with a fluid-like medium confined in a gasket, which is quite often made of rhenium. Besides being one of the strongest materials, diamond is transparent to a wide range of electromagnetic radiation including X-rays and visible light. As one cannot calculate exactly the final pressure achieved in the gasket, an internal pressure standard is required. The positions of the fluorescence lines of ruby are a function of pressure; therefore, ruby fluorescence is very often used for the detection of the actual pressure applied within the cell. Unfortunately ruby fluorescence will not work for cell temperatures above 700 K; therefore, X-ray diffraction is used to measure the lattice spacing of reference materials, where temperature and pressure dependences are known. Different X-ray and Raman investigation techniques are also applied to investigate the pressurized samples.

Higher static temperatures in DACs can be achieved by resistive heating of the total assembly with Ni–Cr heater wires wound around the outer parts of the cell assembly, but this technique is limited in air to about 900 K due to the oxidation of diamond, and in an Ar–H atmosphere up to 1300 K due to ductile deformation in the diamond. To obtain much higher temperatures within DAC, experimental techniques as described in Section A1 (ohmic pulse heating) and A2 (laser-pulse heating) have to be applied within the DAC. The diamond is transparent for visible and infrared light, so the laser light will hit the sample and if the applied energy can be absorbed, the sample will be heated up to temperatures above 3500 K, but only on the side where the laser hits, so quite often a

second heating laser beam will be focused on the opposite side of the sample to avoid large temperature gradients within the sample.

Full ohmic heating of the sample inside the DAC will result in less temperature inhomogeneity within the sample, but additional insulated electrical feed-through and contacting of the sample has to be applied, which is quite complicated. Up to now this technique has been quite rare since a fast pulse heating system has to be incorporated into the DAC-assembly. DAC experiments obtain thermo-physical properties at extreme high pressures and at high temperatures. Further reading is in Refs. [104–107].

A5. Investigations applying shockwaves Shock-physics experiments serve as a primary diagnostic in the determination of the equations-of-state (EOS) that describe solids and liquids at extremely high temperatures and pressures. The EOS of a material specifies a definite relationship between three thermodynamic variables, pressure, temperature, and volume (or density). Thus, it is not possible to adjust the three variables independently. Under dynamic loading, metals can change not only from solid to liquid and liquid to vapour but also from one solid crystal structure to another.

In these experiments a sample, here also called target, made of the material of interest is shock-compressed with high explosives (HE) or through the impact of a flyer plate (projectile) that has been accelerated to a very high velocity, which can be up to 8 km s^{-1}. At impact a compression wave is sent through the target. Flyer plates can be laser-driven, HE-driven, or accelerated in a gas-gun. With all these methods extremely high strains and strain-rates can be achieved in the sample material. The data acquired in such experiments help to constrain the constitutive equations of materials that are then used in numerical simulations. Temperature is an important parameter in these equations but accurate measurement in shock-compression experiments represents a great challenge, in part because of the destructive nature of the experiments and their very short duration of a few microseconds. Shockwave experiments also determine the time-resolved velocity history of a moving surface in a nanosecond timescale, which then can deliver information about the location of phase boundaries.

The obtained equations of state are quite often used to improve the fidelity of large-scale computer simulations of nuclear weapon designs. Further reading is in Refs. [108– 111].

A6. High temperature DSC experiments Differential scanning calorimetry (DSC) allows the characterization of transformation energies as well as measurements of specific heat and is, for moderate temperatures, one of the main investigation techniques, very well explored and described. The top of the $\boldsymbol{C}_P$ sensor holds two crucibles, both with a lid. One experiment has to be divided into three separate runs: First a scan with two empty crucibles to obtain a baseline, second a scan with one crucible containing a reference sample which is usually sapphire, and third a scan with one crucible containing the sample. The $\boldsymbol{C}_P$ sensor is heated within a furnace in a controlled atmosphere. The temperature of the furnace is varied with time. The difference in temperature scans between the reference and the sample is monitored in dependence of the furnace temperature. The heat capacity of the sample, $\boldsymbol{C}_P$, then can be obtained by combining the results of these three temperature dependent scans, when the mass of the reference and of the sample are known [112]. The choice of the correct crucible is here very important; platinum crucibles with ceramic coatings are used or a ceramic crucible is housed in a metallic crucible, which acts as a heat shield and has no direct contact with the sample.

At elevated temperatures, due to the increasing radiative heat transfer from the sensor, which also holds the crucible with the sample, not many instruments are suitable. Instead of the regular platinum wires used as the heating element of the furnace, rhodium wires are used and thus temperatures of 1900 K can be achieved. When using a graphite furnace, a maximum temperature of 2250 K will be obtained. A STA (simultaneous thermal analysis) prototype at PTB Braunschweig, Germany, with tungsten wires for heating will reach temperatures of 2670 K. All the values given within this paragraph are valid for Netzsch-furnaces only [99, 113].

A7. Undercooled liquid samples In order to attain an undercooled liquid state it is necessary to inhibit crystallization. Even with high purity melts contained in a non-reactive crucible that is used for thermophysical property measurement, the amount of undercooling can be severely limited by heterogeneous nucleation at the crucible walls. The application of levitation melting techniques circumvents nucleation at crucible walls, but with bulk liquid volumes the undercooling level can still be limited by internal catalysts or surface films such as oxides. Under these conditions there are two main methods to achieve large undercooling: melt conditioning [114, 115] and melt dispersal into droplets within a suitable carrier fluid [116]. Melt conditioning involves one or all of the following treatments: superheating of the melt prior to cooling, thermal cycling and encasing the melt with a glass coating such as B_2O_3. With these treatments, it is believed that heterogeneous nucleation sites within the melt are dissolved or purged into the glass cover to enable large liquid undercooling that is suitable for property determinations. With melt dispersal the active internal nucleation sites are confined to one portion of the droplet population. The other nucleant-free population will exhibit a

stable, large undercooling. This method is effective when the droplet diameters are about 10 μm or less which implies nucleant concentrations of about 10^{13} m^{-3} and droplet independence is maintained by non-catalytic surface coatings.

Appendix B: Simulation details for MD example We began by creating crystals with 4000 atoms (10 x 10 x 10 unit cells) in the ideal fcc atomic configurations with periodic boundary conditions in all three dimensions. The initial lattice constant was 3.52 A for the Ni simulations and 4.08 A for Au. Note that these do not necessarily represent the equilibrium lattice constants for the interatomic potentials, but finite-temperature relaxation allowed the atoms to move to their relaxed positions during the simulations. The timestep for each run was 0.001 ps (1 fs), and global thermodynamic information (temperature, symmetric pressure tensor and total pressure, potential energy, kinetic energy, total energy, volume and simulation cell dimensions) was written every 1000 steps. Velocities were initialized at 1.0 K with a Gaussian distribution. Every 10 000 steps, per-atom quantities were written. These included positions, velocities, potential and kinetic energies, and centrosymmetry parameter [89]. Restarts were written every 50 000 steps, though they were only used to start the liquid simulations at 2500 K and to restart extended simulations that will be described at the end of this section. Simulations increased and decreased in temperature steps of T = 100 K.

At each temperature, there were several equilibration phases, followed by a production sequence of steps to obtain the data used to calculate average quantities. First the temperature was changed over the course of 50 000 steps in the NPT ensemble, called NPT1. Each dimension was allowed to change independently with a time constant of 10.0 to minimize pressure. The drag on the atoms was set to 2.0 to dampen pressure oscillations that otherwise can be significant in crystals. The thermostat time constant was 1.0.

Following NPT1, we ran 50 000 steps in the NVE (fixed number of atoms, volume and energy) ensemble with a Langevin thermostat to dissipate excess energy in the simulation. The Langevin time constant was 0.1. Following NVE + Lang, we again ran in the NPT ensemble, this time for 25 000 steps and with a drag of 1.0. We finished equilibration by running 25 000 steps of NPT with a drag of 0.0, corresponding to proper Nose–Hoover dynamics.

After the total of 200 000 equilibration steps, we collected production data for 300 000 steps in the same NPT ensemble as the last equilibration phase. For a few cases, we ran an additional 2 000 000 steps (extended simulation) to check whether amorphous phases would crystallize with additional time. The data from the production phases for each temperature were analyzed to determine enthalpies (referenced to the fcc crystal at 300 K), resulting heat capacities ($\boldsymbol{C}_P = \partial \boldsymbol{H}/\partial \boldsymbol{T}\,|_p$), and structure (including centrosymmetry parameter and common neighbour analysis). The common neighbour analysis (CNA) [88] was done in OVITO [117].

Acknowledgements We would like to acknowledge the organizers of the 2013 Ringberg Unaries Workshop. We would also like to thank Mark Asta for a very careful read of this manuscript and his associated feedback and suggestions. Q.C. would like to thank Prof. Wilde for kindly providing data values of Au in his publication. J.H.P. gratefully acknowledges the support from ONR (N00014-12-1-0569).

NIST does not endorse any commercial products, and use of these products does not imply endorsement by NIST.

References

[1] A. T. Dinsdale, Calphad **15**, 317 (1991).

[2] J. Agren, B. Cheynet, M. T. Clavaguera-Mora, K. Hack, J. Hertz, F. Sommer, and U. Kattner, Calphad **19**, 449 (1995).

[3] R. DeHoff, Thermodynamics in Materials Science, second ed. (CRC Press, Boca Raton, 2006), p. 163.

[4] J. Agren, Phys. Chem. Liq. **18**, 123 (1988). [5] G. Grimvall, Phys. Scr. **11**, 381 (1975)

[6] B. Sadigh and G. Grimvall, Phys. Rev. B **54**, 15742 (1996).

[7] M. Forsblom and G. Grimvall, Phys. Rev. B **72**, 132204 (2005).

[8] T. M. Brown and J. B. Adams, J. Non-Cryst. Solids **180**, 275 (1995).

[9] C. A. Becker and M. J. Kramer, Modell. Simul. Mater. Sci. Eng. **18**, 074001 (2010).

[10] L. Bosio, R. Cortes, and A. Deftain, J. Chim. Phys. (France) **70**, 357 (1973).

[11] Y. Takahashi, H. Kadokura, and H. Yokokawa, J. Chem. Thermodyn. **15**, 65 (1983).

[12] J. H. Perepezko and J. S. Paik, J. Non-Cryst. Solids **61**, 125 (1984).

[13] S. S. Chang and A. B. Bestul, J. Chem. Thermodyn. **6**, 325 (1974).

[14] F. Grønvold, J. Chem. Thermodyn. **5**, 525 (1973).

[15] G. Wilde, J. Non-Cryst. Solids **307–310**, 853 (2002).

[16] M. E. Schlesinger and S. Jacob, J. Opt. Mater. **56**(12), 37 (2004).

[17] H. P. Wang and B. Wei, Appl. Phys. A **95**, 661 (2009).

[18] X. J. Han, M. Chen and Z. Y. Guo, J. Phys.: Condens. Matter **26**, 705 (2004).

[19] Y. J. Lv and M. Chen, Int. J. Mol. Sci. **12**, 278 (2011).

[20] N. Jakse and A. Pasturel, J. Chem. Phys. **120**, 6124 (2004).

[21] N. Jakse and A. Pasturel, J. Chem. Phys. **123**, 244512 (2005).

[22] W. Kauzmann, Chem. Rev. **43**, 219 (1948).

[23] H. S. Chen and D. Turnbull, J. Chem. Phys. **48**, 2650 (1968).

[24] H. B. Ke, P. Wen, D. Q. Zhao and W. H. Wang, Appl. Phys. Lett. **96**, 251902 (2010).

[25] S. Sastry, Nature **409**, 164 (2001).

[26] P. G. Debenedetti, T. M. Truskett, C. P. Lewis, and F. H. Stillinger, Adv. Chem. Eng. **28**, 21 (2001).

[27] A. Heuer, J. Phys.: Condens. Matter **20**, 373101 (2008).

[28] F. Sciortino, J. Stat. Mech. P05015 (2005).

[29] W. L. Johnson and K. Samwer, Phys. Rev. Lett. **95**, 195501 (2005).

[30] F. Spaepen and D. Turnbull, Annu. Rev. Phys. Chem. **35**, 241 (1984).

[31] M. H. Cohen and G. S. Grest, Phys. Rev. B **20**, 1077 (1979).

[32] C. A. Angell and C. T. Moynihan, Metall. Mater. Trans. B **31B**, 587 (2000).

[33] S. G. Hao, C. Z. Wang, M. Li, R. E. Napolitano, M. I. Mendelev, and K. M. Ho, Comput. Mater. Sci. **49**, 615 (2010).

[34] S.-T. Lin, M. Blanco, and W. A. Goddard III, J. Chem. Phys. **119**, 11792 (2003).

[35] G. Zhang, Q. An, and W. A. Goddard III, J. Phys. Chem. C **115**, 2320 (2011).

[36] Q. An, K. Samwer, W. A. Goddard III, W. L. Johnson, A. Jaramillo-Botero, G. Garret, and M. D. Demetriou, J. Phys. Chem. Lett. **3**, 3143 (2012).

[37] Y. Q. Cheng and E. Ma, Prog. Mater. Sci. **56**, 379 (2011).

[38] R. Bormann, Mater. Sci. Eng. **A178**, 55 (1994).

[39] R. Bormann performed pioneering work in the thermody-namics of metallic glases before he died suddenly in January 2013.

[40] G. Shao, B. Lu, Y. Q. Liu, and P. Tsakiropoulos, Inter-metallics **13**, 409 (2005).

[41] M. Baricco and M. Palumbo, Adv. Eng. Mater. **9**, 454 (2007).

[42] M. Palumbo and L. Battezzati, Calphad **32**, 295 (2008).

[43] S. B. Thomas and G. S. Parks, J. Phys. Chem. **35**, 2091 (1931).

[44] N. E. Shmidt, Russ. J. Inorg. Chem. **11**, 241 (1966).

[45] P. Richet, D. de Ligny, and E. F. Westrum, Jr., J. Non-Cryst. Solids **315**, 20 (2003).

[46] S. A. Decterov, V. Swamy, and I.-H. Jung, Int. J. Mater. Res. **98**, 987 (2007).

[47] B. Jonsson and J. Agren, Metall. Trans. A **17A**, 607 (1986).

[48] A. D. Pelton, M. Blander, M. T. Clavaguera-Mora, M. Hoch, Hoglund,¨ H. L. Lukas, P. Spencer, and B. Sundman, Calphad **21**, 155 (1997).

[49] E. Brosh, A. D. Pelton, and S. A. Decterov, Int. J. Mater. Res. **103**, 494 (2012).

[50] A. N. Grundy, H.-C. Liu, I.-H. Jung, S. A. Decterov, and A. Pelton, Int. J. Mater. Res. **99**, 1185 (2008).

[51] A. N. Grundy, I.-H. Jung, A. D. Pelton, and S. A. Decterov, Int. J. Mater. Res. **99**, 1195 (2008).

[52] W.-Y. Kim, A. D. Pelton, and S. A. Decterov, Int. J. Mater. Res. **103**, 313 (2012).

[53] E. Brosh, A. D. Pelton, and S. A. Decterov, Int. J. Mater. Res. **103**, 537 (2012).

[54] R. M. Martens, M. Rosenhauer, H. Buettner, and K. Von Gehlen, Chem. Geol. **62**, 49 (1987).

[55] P. Richet and Y. Bottinga, Rev. Geophys. **24**, 1 (1986).

[56] D. Turnbull, Contemp. Phys. **10**, 473 (1969).

[57] C. H. Shomate, J. Phys. Chem. **58**, 368 (1954).

[58] NIST Chemistry Webbook. http://webbook.nist.gov/chemistry/

[59] M. Hoch, High Temp. High Press. **1**, 531 (1969).

[60] Q. Chen and B. Sundmann, J. Phase Equilib. **22**, 631 (2001).

[61] B. Jonsson and J. Agren, J. Less-Common Metals **145**, 153 (1988).

[62] O. Tolochko and J. Agren, J. Phase Equilib. **21**, 19 (2000).

[63] Q. Chen, unpublished (2013).

[64] J. Hirschfelder, D. Steveson, and H. Eyring, J. Chem. Phys. **5**, 896 (1937).

[65] G. Pottlacher, High Temperature Thermophysical Properties of 22 Pure Metals (Edition Keiper, Graz, 2010).

[66] J. W. Tester, R. C. Feber, and C. C. Herrick, J. Chem. Eng. Data **13**, 419 (1968).

[67] A. I. Taub and F. Spaepen, Acta Metall. **28**, 1781 (1980) [68] M. H. Cohen and D. Turnbull, J. Chem. Phys. **31**, 1164 (1959)

[69] K. Lejaeghere, V. Van Speybroeck, G. Van Oost, and S. Cottenier, Crit. Rev. Solid State Mater. Sci. **39**, 1 (2014).

[70] G. Kresse and J. Hafner, Phys. Rev. B **47**, 558 (1993).

[71] G. Kresse and J. Hafner, Phys. Rev. B **49**, 14251 (1994).

[72] D. Alfe,´ M. J. Gillan, and G. D. Price, J. Chem. Phys. **116**, 6170 (2002).

[73] M. Asta, V. Ozolins, J. J. Hoyt, and M. van Schilfgaarde, Phys. Rev. B **64**, 020201(R) (2001).

[74] J. C. Slater and G. F. Koster, Phys. Rev. **94**, 1498 (1954).

[75] C. M. Goringe, D. R. Bowler, and E. Hernandez,` Rep. Prog. Phys. **60**, 1447 (1997).

[76] D. Frenkel and B. Smit, Understanding Molecular Sim-ulation: From Algorithms to Applications, second ed. (Academic Press, San Diego, 2001).

[77] C. A. Becker, F. Tavazza, Z. T. Trautt, and R. A. Buarque de Macedo, Curr. Opin. Solid State Mater. Sci. **17**, 277–283 (2013).

[78] M. S. Daw and M. I. Baskes, Phys. Rev. Lett. **50**, 1285 (1983).

[79] M. S. Daw and M. I. Baskes, Phys. Rev. B **29**, 6443 (1984).

[80] S. M. Foiles, M. I. Baskes, and M. S. Daw, Phys. Rev. B **33**, 7983 (1986).

[81] M. W. Finnis and J. E. Sinclair, Philos. Mag. A **50**, 45 (1984).

[82] G. Grochola, S. P. Russo, and I. K. Snook, J. Chem. Phys. **123**, 204719 (2005).

[83] G. J. Ackland, G. I. Tichy, V. Vitek, and M. W. Finnis, Philos. Mag. A **56**, 735 (1987).

[84] G. P. Purja Pun and Y. Mishin, Philos. Mag. **89**, 3245 (2009).

[85] M. I. Mendelev, M. J. Kramer, S. G. Hao, K. M. Ho, and C.Wang, Philos. Mag. **92**, 4454 (2012).

[86] Y. Mishin, Acta Mater. **52**, 1451 (2004).

[87] S. Plimpton, J. Comput. Phys. **117**, 1 (1995). http://lammps.sandia.gov

[88] J. D. Honeycutt and H. C. Andersen, J. Phys. Chem. **91**, 4950 (1987).

[89] C. L. Kelchner, S. J. Plimpton, and J. C. Hamilton, Phys. Rev. B **58**, 11085 (1998).

[90] F. Kirchhoff, M. J. Mehl, N. I. Papanicolaou, D. A. Papa-constantopoulos, and F. S. Khan, Phys. Rev. B **63**, 195101 (2001).

[91] G. Wilde, C. Mitsch, G. P. Gorler, and R. Willnecker, J. Non-Cryst. Solids **205–207**, 425 (1996).

[92] C. J. Smithell, in: Smithells Metals Reference Book, edited by E. A Brandes and G. Brook (Butterworths, London, 1992), pp. 8-41 to 8-54.

[93] T. Iida and R. I. L. Guthrie, The Physical Properties of Liquid Metals (Clarendon, Oxford, 1993), pp. 91, 201, 213.

[94] G. Pottlacher, E. Kaschnitz, and H. Jager,¨ J. Non-Cryst. Solids **156–158**, 374 (1993).

[95] M. Barth, F. Joo, B. Wei, and D. M. Herlach, J. Non-Cryst. Solids **156–158**, 398 (1993).

[96] K. Schaefers, M. Rosner¨-Kuhn, and M. G. Frohberg, Mater. Sci. Eng. A **197**, 83 (1995).

[97] C. Cagran and G. Pottlacher, in: The Handbook of Ther-mal Analysis & Calorimetry, Vol. 5, Further Advances, Techniques and Applications (Elsevier, Amsterdam, 2007), edited by M.E. Brown and P.K. Gallagher, chap. 14.

[98] G. Pottlacher, K. Aziz, and A. Schmon, High Temp. High Press. **41**, 377 (2012).

[99] H. Suga, G. Pottlacher, and I. Egry, in: IUPAC Exper-imental Thermodynamics, Vol. VI. Measurement of the Thermodynamic Properties of Single Phases, edited by A.H. Goodwin, K. N. Marsh, and W. A. Wakeham (Elsevier, Amsterdam, 2003), Section 10, “Extreme Conditions", pp. 475–536.

[100] F. De Bruycker, K. Boboridis, D. Manara, P. Poml,¨ M. Rini, J. M. Konings, Mater. Today **13**, 53 (2010).

[101] G. Pottlacher, in: Concise Encyclopedia of Materials Char-acterization, edited by R. W. Cahn (Pergamon Press, Oxford, 1993), p. 525.

[102] T. Baykara, R. H. Hauge, N. Norem, P. Lee, and J. J. Mar-grave, High Temp. Sci. **32**, 113 (1991).

[103] D. M. Herlach, R. F. Cochrane, I. Egry, H. J. Fecht, and A. Greer, Int. Mater. Rev. **38**, 273 (1993).

[104] D. J. Dunstan and I. L. Spain, J. Phys. E, Sci. Instrum. **22**, 913 (1989).

[105] I. L. Spain and D. J. Dunstan, J. Phys. E, Sci. Instrum. **22**, 923 (1989).

[106] Z. M. Geballe and R. Jeanloz, J. Appl. Phys. **111**, 123518 (2012).

[107] C. S. Zha and W. A. Basset, Rev. Sci. Instrum. **74**, 1255 (2003).

[108] R. S. Hixson, G. T. Gray, and D. B. Hayes, Los Alamos Sci. **28**, 115 (2003).

[109] K. Boboridis, A. Seifter, and A. W. Obst, High-Speed Infrared Pyrometry for Surface Temperature Measurements on Shocked Solids, VDI-Berichte Nr. 1784 (VDI Verlag, Dusseldorf,¨ 2003), pp. 119–126.

[110] A. Seifter, M. R. Furlanetto, M. Grover, D. B. Holtkamp, S. Macrum, A. W. Obst, J. R. Payton, J. B. Stone, G. D. Stevens, D. C. Swift, L .J. Tabaka, W. D. Turley, and L. R. Veeser, J. Appl. Phys. **105**, 123526 (2009).

[111] B. J. Jensen, G. T. Gray, and R. S. Hixson, J. Appl. Phys. **105**, 103502 (2009).

[112] M. Baricco, I. Battezzati, and P. Rizzi, J. Alloys Compd. **220**, 212 (1995).

[113] B. Wilthan, private communication (2013).

[114] J. Fehling and E. Scheil, Z. Metallkd. **53**, 593 (1962).

[115] G. Wilde, J. L. Sebright, and J. H. Perepezko, Acta Mater. **54**, 4759 (2006).

[116] J. H. Perepezko, B. A. Mueller, and K. Ohsaka, in: Under-cooled Alloy Phases, edited by E. W. Collings and C. C. Koch (TMS-AIME, Warrendale, 1987), p. 289.

[117] A. Stukowski, Modell. Simul. Mater. Sci. Eng. **18**, 015012 (2010).

[118] I. Mills, T. Cvitas,˘ K. Homann, N. Kallya, and K. Kuchitsu, Quantities, Units and Symbols in Physical Chemistry, second ed. (Blackwell Science, Oxford, 1993); www.iupac.org/publications/books/gbook/green book 2ed. pdf.